



# Application of NEAMS Multiphysics Framework for Species Tracking in Molten Salt Reactors

August 2023

*DOE Molten-Salt Reactor Campaign  
Milestone M3RD-23IN0602011*

Samuel Walker, Mauricio Tano, and Abdalla Abou-Jaoude  
*Idaho National Laboratory*



*INL is a U.S. Department of Energy National Laboratory  
operated by Battelle Energy Alliance, LLC*

**DISCLAIMER**

This information was prepared as an account of work sponsored by an agency of the U.S. Government. Neither the U.S. Government nor any agency thereof, nor any of their employees, makes any warranty, expressed or implied, or assumes any legal liability or responsibility for the accuracy, completeness, or usefulness, of any information, apparatus, product, or process disclosed, or represents that its use would not infringe privately owned rights. References herein to any specific commercial product, process, or service by trade name, trade mark, manufacturer, or otherwise, does not necessarily constitute or imply its endorsement, recommendation, or favoring by the U.S. Government or any agency thereof. The views and opinions of authors expressed herein do not necessarily state or reflect those of the U.S. Government or any agency thereof.

# **Application of NEAMS Multiphysics Framework for Species Tracking in Molten Salt Reactors**

**DOE Molten-Salt Reactor Campaign  
Milestone M3RD-23IN0602011**

**Samuel Walker, Mauricio Tano, and Abdalla Abou-Jaoude  
Idaho National Laboratory**

**August 2023**

**Idaho National Laboratory  
Idaho Falls, Idaho 83415**

**<http://www.inl.gov>**

**Prepared for the  
U.S. Department of Energy  
Office of Nuclear Energy  
Under DOE Idaho Operations Office  
Contract DE-AC07-05ID14517**

*Page intentionally left blank*




INL ART Program

# Application of NEAMS Multiphysics Framework for Species Tracking in Molten Salt Reactors

INL/RPT-23-74376  
Revision 0

August 2023

Technical Reviewer: (Confirmation of mathematical accuracy, and correctness of data and appropriateness of assumptions.)

  
\_\_\_\_\_  
Parikshit Bajpai  
Molten Salt Modeling and Simulation Scientist

08/24/2023  
\_\_\_\_\_  
Date

Approved by:

*M. Davenport*  
\_\_\_\_\_  
Michael E. Davenport  
ART Project Manager

8/24/2023  
\_\_\_\_\_  
Date

  
\_\_\_\_\_  
Michelle T. Sharp  
INL Quality Assurance

8/24/2023  
\_\_\_\_\_  
Date

## ABSTRACT

This report from Idaho National Laboratory (INL) summarizes the key modeling and simulation activities conducted under the Department of Energy (DOE) Molten Salt Reactor (MSR) Campaign during the Fiscal Year 2023 (FY23). The focus of the work was to leverage state-of-the-art modeling capabilities from the DOE Nuclear Energy Advanced Modeling and Simulation (NEAMS) codes to enable novel multiphysics and multiscale modeling and simulation of MSRs.

Through collaboration with NEAMS code developers, advanced multiphysics analysis capabilities for MSR systems were demonstrated by coupling depletion, thermal-hydraulics, and thermochemistry into an innovative framework for chemical species transport in MSRs. As a result, the framework can track nuclides throughout their lifetimes in the core, from production (depletion) to advection throughout the salt volume (thermal-hydraulics) and off-gassing or precipitation outside of the salt (thermochemistry).

This work supports the near-term deployment of MSRs by integrating the synergistic efforts between the DOE's MSR Campaign and NEAMS program. The resulting framework will help better connect system design modelers with experimentalists to better understand and predict complex physical behaviors in MSRs. Researchers and MSR developers alike can now leverage these new modeling and simulation capabilities to perform novel analyses with applications including:

- MSR dynamics during normal operational transients and accident scenarios
- Off-gas system design and performance for fuel cycle and depletion analysis
- Corrosion and active chemistry control for reactor component health and lifetime determination
- Source term, decay heat and activity determination in accident scenarios
- Special nuclear material accountancy and chemical forensic analysis for safeguards
- Digital twin development of experiments and experimental reactor demonstrations
- Measurement requirements for instrumentation and control design
- Uncertainty and sensitivity analysis of missing data to inform future experimental data collection.

*Page intentionally left blank*

## ACKNOWLEDGEMENTS

This manuscript was drafted on behalf of Idaho National Laboratory, operated by Battelle Energy Alliance, LLC, under contract no. DE-AC07-05ID14517 with the U.S. Department of Energy (DOE). This work was prepared for the U.S. DOE Office of Nuclear Energy (DOE-NE) via funding by the MSR Campaign. It made use of the resources of the High-Performance Computing Center at Idaho National Laboratory, which is supported by the Office of Nuclear Energy of the U.S. Department of Energy and the Nuclear Science User Facilities under contract no. DE-AC07-05ID14517.

The authors would like to thank the MSR Campaign National Technical Director (NTD) Patricia Paviet for sponsoring this work and enthusiastically supporting it.

In addition, the authors would like to acknowledge the contributions of Theodore Besmann and his team in developing the Molten Salt Thermophysical Database—Thermochemical (MSTDB-TC) that was leveraged extensively in these studies.

The authors would also like to acknowledge the contributions of Markus Piro and his team developing the open-source thermochemistry solver Thermochemica, as well as Parikshit Bajpai and Daniel Schwen who helped integrate this new modeling capability into the existing NEAMS toolset for thermochemistry calculations.

Last, the authors would like to thank Chandrakanth Bolisetti, who provided an MSFR mesh used in some of these analyses, along with Gerhard Strydom, Amy Boll, Michelle Sharp, Barney Hadden, and Nikki Peterson for reviewing and providing editorial support of this technical report.

*Page intentionally left blank*

# CONTENTS

ABSTRACT.....	v
ACKNOWLEDGEMENTS.....	vii
ACRONYMS.....	xii
1. INTRODUCTION.....	1
2. IMPORTANCE OF CHEMICAL-SPECIES TRANSPORT IN MSRS.....	5
2.1. Definition of the Redox Potential in Relation to the Fluorine or Chlorine Potential.....	5
2.2. Chemical-Species Transport and Fuel-Salt Redox Potential.....	5
2.3. Chemical Species Transport in the Molten Salt Reactor Experiment.....	6
2.3.1. Understanding Relative Redox Potentials of Reactions.....	6
2.3.2. Changing Redox Potential in the MSRE.....	8
3. MULTIPHYSICS-FRAMEWORK APPROACH.....	9
3.1. Griffin Depletion.....	11
3.2. Pronghorn Species Transport.....	12
3.3. Thermochemica Chemical Equilibrium.....	13
3.4. Selected Applications of Chemical Species Transport in MSRs.....	14
3.4.1. Chemical Speciation and Off-Gas Analysis.....	14
3.4.2. Corrosion and Active Chemistry Control Analysis.....	15
4. DEPLETION-DRIVEN THERMOCHEMISTRY (GRIFFIN + THERMOCHIMICA).....	16
4.1. Zero-Dimensional Chemical Speciation and Off-Gas Analysis.....	18
4.1.1. Fluoride Fuel Salt Analysis.....	18
4.1.2. Chloride Fuel Salt Analysis.....	20
4.2. Zero-dimensional Corrosion and Active Chemistry Control Analysis.....	22
4.2.1. Fluoride Fuel-Salt Analysis.....	22
4.2.2. Chloride Fuel-Salt Analysis.....	24
5. SPATIALLY RESOLVED THERMOCHEMISTRY (PRONGHORN + THERMOCHIMICA).....	27
5.1. Spatially Resolved Chemical Speciation and Off-Gas Analysis.....	29
5.2. Spatially Resolved Corrosion and Active-Chemistry Control.....	32
6. NEAMS FRAMEWORK: DEPLETION-DRIVEN SPATIALLY RESOLVED THERMOCHEMISTRY (GRIFFIN + PRONGHORN + THERMOCHIMICA).....	36
7. FUTURE WORK AND SYNERGISTIC COLLABORATIONS.....	41
7.1. Validation of Framework via MSRE Data using MSTDB V3.0.....	41
7.2. Informing and Coupling with System-Code Analysis.....	41
7.3. Framework Enhancements and New Applications.....	41

7.4. Future Work for Later Years.....	41
8. SUMMARY AND CONCLUSIONS.....	42
9. REFERENCES.....	42

## FIGURES

Figure 1-1. Chemical species transport examples in MSR systems.....	1
Figure 1-2. NEAMS based multiphysics and multiscale framework for MSR analysis.....	2
Figure 2-1. UF <sub>4</sub> to UF <sub>3</sub> ratio during the <sup>235</sup> U MSRE runs (reformatted from [12]). .....	8
Figure 3-1. NEAMS based multiphysics and multiscale framework for chemical species transport in MSRs. ....	10
Figure 3-2. Depletion-driven volatilization of gaseous species to off-gas system.....	14
Figure 3-3. Depletion-driven corrosion of structural materials and active chemistry control. ....	15
Figure 4-1. Depletion-driven thermochemistry code coupling.....	17
Figure 4-2. Change in fluorine potential over 60 days or 2.87 MWd/Kg-U burnup. ....	18
Figure 4-3. Changes in element vapor pressures in the fluoride fuel salt over 60 days or 2.87 MWd/Kg-U burnup. ....	19
Figure 4-4. Change in chlorine potential over 60 days or 2.87 MWd/Kg-U burnup. ....	20
Figure 4-5. Changes in element vapor pressures in the chloride fuel salt over 60 days or 2.87 MWd/Kg-U burnup. ....	21
Figure 4-6. Change in fluorine/redox potential over 3.11 MWd/Kg-U burnup, with no redox control and with a PID controller. ....	23
Figure 4-7. Change in corrosion-product formation over 3.11 MWd/Kg-U burnup, with no redox control and with a PID controller. ....	23
Figure 4-8. Off-gas build up in fluoride fuel salt system over 3.11 MWd/Kg-U burnup with no redox potential control and with PID controller. ....	24
Figure 4-9. Change in chlorine/redox potential over 3.11 MWd/Kg-U burnup with no redox control and with a PID controller. ....	25
Figure 4-10. Change in corrosion product formation over 3.11 MWd/Kg-U burnup with no redox potential control and with PID controller. ....	25
Figure 4-11. Off-gas buildup in chloride fuel salt system over 3.11 MWd/Kg-U burnup with no redox potential control and with PID controller. ....	26
Figure 5-1. Spatially resolved thermochemistry code coupling.....	28
Figure 5-2. (Left) temperature field (K) and (right) pressure field (Pa). ....	28
Figure 5-3. Velocity fields (m/s) in (left) x-direction and (right) y-direction.....	29
Figure 5-4. Xenon-137 distribution (mol) in the MSFR at (clockwise, from upper left) 0, 50, 100, and 150 s, respectively, showcasing decrease of gaseous species due to extraction (extraction boundary at top of upper plenum). ....	30

Figure 5-5. Cesium-137 (mol) distribution in MSFR at (clockwise, from upper left) 0, 50, 100, and 150 s, respectively, showcasing decrease of daughter species due to parent extraction (extraction boundary at top of upper plenum). .....	31
Figure 5-6. Vapor pressure (atm) of (left) CsI and (right) I <sub>2</sub> in the MSFR, showcasing relative decrease of Cs and relative increase of I vapor pressure at boundary. ....	32
Figure 5-7. Be distribution (mol) at (clockwise, from upper left) 0, 50, 100, and 150 s, respectively, showcasing beryllium addition to MSFR system (inlet at bottom of lower plenum). .....	33
Figure 5-8. Corresponding fluoride (F-) potential (J/mol) at (clockwise, from upper left) 0, 50, 100, and 150 s, respectively, showcasing beryllium reduction of MSFR fuel salt – inlet at bottom of lower plenum. ....	34
Figure 5-9. Corresponding NiF <sub>2</sub> distributions (mol) at (clockwise, from upper left) 0, 50, 100, and 150 s, respectively, showcasing loss of NiF <sub>2</sub> to Ni <sub>(s)</sub> precipitant due to beryllium addition reducing MSFR fuel salt. ....	35
Figure 6-1. Depletion-driven spatially resolved thermochemistry code coupling. ....	36
Figure 6-2. Fluoride (F-) potential (J/mol) at (clockwise, from upper left) 0.024, 0.048, 0.096, and 0.239 MWd/Kg-U, showcasing the oxidizing effect of depletion on MSFR fuel salt. ....	37
Figure 6-3. NiF <sub>2</sub> distributions (mol) at (clockwise, from upper left) 0.024, 0.048, 0.096, and 0.239 MWd/Kg-U, showcasing gain of NiF <sub>2</sub> due to depletion oxidation. ....	38
Figure 6-4. Vapor pressure (atm) of CsI distributions at (clockwise, from upper left) 0.024, 0.048, 0.096, and 0.239 MWd/Kg-U, showcasing volatilizing effect of depletion. ....	39
Figure 6-5. I <sub>2</sub> vapor pressure [atm] distributions at (clockwise, from upper left) 0.024, 0.048, 0.096, and 0.239 MWd/Kg-U, showcasing volatilizing effect of depletion. ....	40

## TABLES

Table 1-1. Possible applications of state-of-the-art framework for MSRs. ....	3
Table 2-1. Calculated electrode potential in LiF-LiF-0.33 BeF <sub>2</sub> (1000 K) (reformatted from [7]). ....	7
Table 4-1. Generic reactor specifications. ....	17
Table 4-2. Off-gas comparison: analysis of <sup>137</sup> Cs and <sup>131</sup> I in the fluoride and chloride reactors with and without PID redox-potential control. ....	26
Table 6-1. <sup>137</sup> Cs off-gas analysis after 3.11 MWd/Kg-U burnup of fluoride fuel salt. ....	40



## ACRONYMS

ANL	Argonne National Laboratory
BV	Butler-Volmer
CRM	Chemical Reaction Module
DOE	Department of Energy
EOS	Equation of state
FP	Fission product
FY	Fiscal year
INL	Idaho National Laboratories
GEM	Gibbs energy minimizer
MCRE	Molten Chloride Reactor Experiment
MOOSE	Multiphysics Object Oriented Simulation Environment
MSFR	Molten-salt fast reactor
MSTDB	Molten Salt Thermodynamic Database
MSR	Molten Salt Reactor
MSRE	Molten Salt Reactor Experiment
NEAMS	Nuclear Energy Advanced Modeling and Simulation
NTD	National technical director
ORNL	Oak Ridge National Laboratory
PID	Proportional-integral-derivative
PNP	Poisson-Nernst-Planck
SAM	System Analysis Module
THM	Thermal Hydraulics Module
VTB	Virtual Test Bed

# Application of NEAMS Multiphysics Framework for Species Tracking in Molten Salt Reactors

## 1. INTRODUCTION

The Department of Energy's (DOE's) Molten Salt Reactor (MSR) Campaign supports the development and near-term deployment of liquid-fuel molten-salt-based systems by addressing technological challenges and the knowledge gaps. The program has funded cutting-edge research in modeling and experimentation to address these challenges through collaboration and integration of efforts within the DOE complex.

By having molten salt play both the role of fuel and coolant simultaneously, the physics of liquid-fuel MSRs are intrinsically and tightly coupled. A key knowledge gap and resulting technological challenge lies in the realm of chemical-species transport in MSRs, shown in Figure 1-1. This process involves nuclide generation, decay, and transmutation due to depletion, which shifts the elemental composition and thermochemistry of the MSR system throughout the reactor lifetime. Slow changes in the pseudo chemical equilibrium of the system alter the chemical speciation of volatile fission products (FPs) like cesium-iodide gas which can transport, deposit, and diffuse into porous structural materials or into off-gas systems as seen in Figure 1-1.

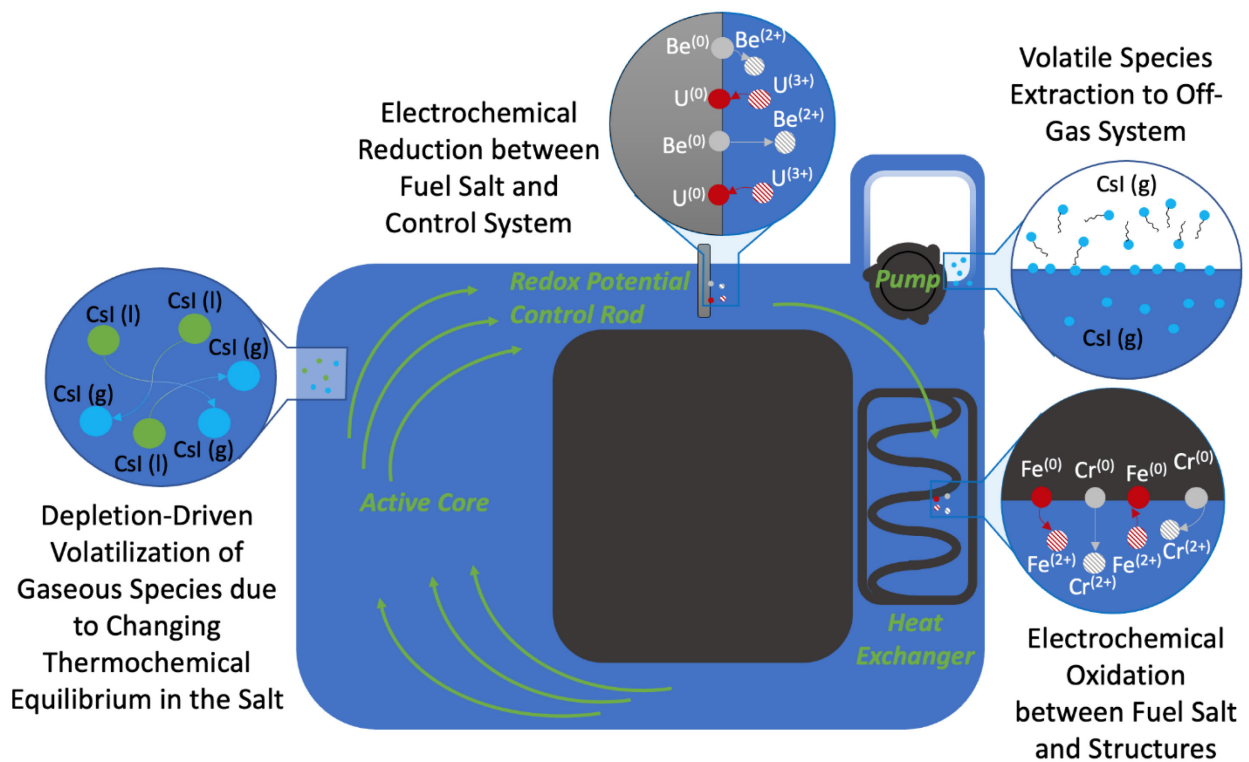


Figure 1-1. Chemical species transport examples in MSR systems.

Additionally, changes in salt composition with depletion drives subsequent changes in the chemical potential of the base ion in a molten salt (e.g., F or Cl). This can dictate corrosion via electrochemical oxidation of structural alloys containing chromium and iron. Active-chemistry or redox-potential control of the fuel salt is another key process that alters the chemical equilibrium of the fuel salt and thereby controls the multiphysics behavior of the reactor during normal reactor operation. It is an important initial condition for accident scenarios.

Developing multiphysics models that adequately capture these phenomena is a critical requirement for both system-design engineers via simulation and for experimentalists to inform the measurement requirements of instrumentation used for reactor control via auxiliary systems—i.e., off-gas and chemistry-control systems. The work detailed in this milestone is a crucial step forward in resolving this issue through the development of a state-of-the-art framework for multiphysics and multiscale modeling of MSRs that adequately couples the multiple phenomena integral to controlling MSR system behavior.

This milestone summarizes recent progress made in advanced modeling and simulation of MSRs accomplished under the MSR Campaign at Idaho National Laboratory (INL). This work leverages the latest experimental data generated and collated within the campaign and can further provide feedback to experimentalists regarding data needs and instrumentation requirements. The focus of the work was to develop a multiphysics and multiscale framework for MSR analysis and chemical-species transport using the DOE’s Nuclear Energy Advanced Modeling and Simulation (NEAMS) suite of tools, shown in Figure 1-2.

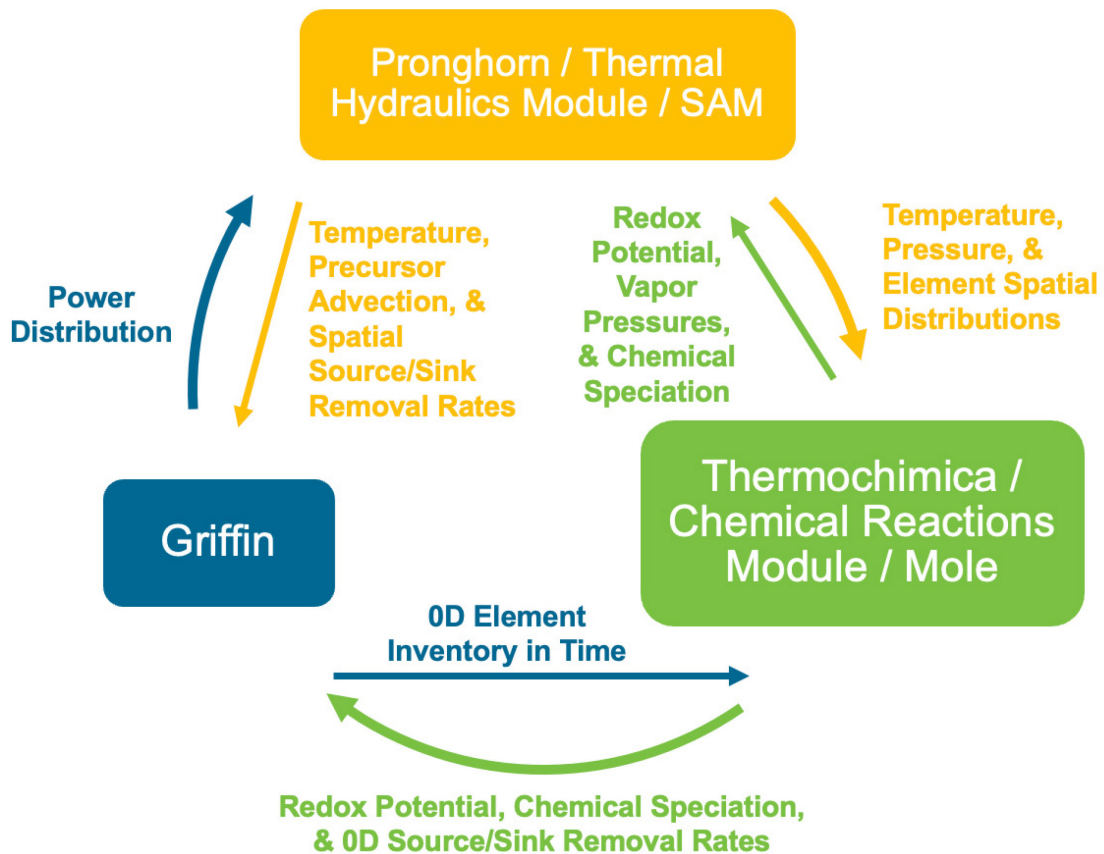


Figure 1-2. NEAMS based multiphysics and multiscale framework for MSR analysis.

The resulting framework allows detailed analysis in the following applications essential to MSR technology development, design, and operation, as shown in Table 1-1.

Table 1-1. Possible applications of state-of-the-art framework for MSRs. Applications 2 and 3 highlighted because they were the primary focus for this report.

NEAMS-based Framework	Specific MSR Analysis Applications
Application 1	MSR dynamics during normal operational transients and accident scenarios
Application 2	<b>Off-gas system design and performance for fuel cycle and depletion analysis</b>
Application 3	<b>Corrosion and active chemistry control for reactor component health and lifetime determination</b>
Application 4	Source term, decay heat, and activity determination in accident scenarios
Application 5	Special nuclear material accountancy and chemical forensic analysis for safeguards
Application 6	Uncertainty and sensitivity analysis of missing data to inform future experimental data collection.
Application 7	Measurement requirements for instrumentation and control design
Application 8	Digital twin development of experiments and experimental reactor demonstrations

Two of these applications were simulated using the framework as a proof of concept to showcase the new analysis capability. Building upon recent work accomplished in Fiscal Year (FY)-22, Applications 2 and 3—chemical species transport to an off-gas system and corrosion and active chemistry control (shown in bold on Table 1-1)—were selected and investigated as the framework was assembled by coupling the various NEAMS codes.

This work has seven direct benefits to the MSR campaign. It:

1. Builds an unparalleled modeling and simulation capability to evaluate fuel depletion, thermochemical equilibrium, and chemical-species transport in MSRs using NEAMS tools. This is critical for the analysis applications listed above.
2. Identifies gaps in thermochemical data and remaining modeling needs for chemical-species transport in MSR systems.
3. Provides a multiphysics method to determine instrumentation measurement sensitivity requirements for MSR campaign experimentalists.
4. Provides a framework that can be leveraged for uncertainty/sensitivity analysis to further inform experimental work and data collection prioritization.
5. Prescribes a multiscale method to inform system-level transport models and identifies ways to couple these analyses to existing framework.
6. Provides a multiphysics coupled method to evaluate corrosion-product formation and chemical-species volatilization occurring in MSR systems, given reactor-depletion history and active-chemistry control.
7. Encourages framework adoption to accelerate innovation within the MSR campaign and enhance interactions and collaborations with industry by leveraging DOE-sponsored tools.

The key outcomes of the work have been published incrementally as the framework was developed and analyses were performed. This work resulted in three academic conference papers, one journal publication, and one remaining journal publication currently under preparation [1–4].

#### WORK RELATED PUBLICATIONS

The work focused on this framework development and analysis resulted in four publications listed below with a fifth publication under preparation.

##### Conference Publications:

1. S. A. WALKER, M. E. TANO, and A. ABOU-JAOUDE, “Leveraging Coupled Thermochemical Depletion Capabilities to Evaluate Off Gas and Source Term Characterization in Molten Salt Reactor Systems,” *Proc. Intl. Cong. Adv. Nucl. Pow. Plnts. (ICAPP 2023)*, Gyeongju, South Korea, April 23–27, 2023, Paper #1334 (2023).
2. S. A. WALKER, M. E. TANO, and A. ABOU-JAOUDE, “A Coupled Griffin and Thermochemical Method for Redox Potential Control and Off-Gas Analysis During Depletion in Molten Salt Reactors,” *Proc. Intl. Conf. Math. Comp. Mthds. Nucl. Sci. Eng. (M&C 2023)*, Niagara Falls, Ontario, Canada, August 13–17, 2023, Accepted for Publication (2023).
3. S. A. WALKER, P. BAJPAI, D. SCHWEN, M. E. TANO, and A. ABOU-JAOUDE, “Spatially Resolved Thermochemistry with Chemical Species Tracking in Molten Salt Reactors,” *Trans. Am. Nucl. Soc. (Winter Meeting 2023)*, Washington D.C., November 12–15, 2023, [Summary submitted for publication] (2023).

##### Journal Publications:

1. S. A. WALKER, M. E. TANO, A. ABOU-JAOUDE, and O. CALVIN, “Depletion-driven thermochemistry of molten salt reactors: review, method, and analysis,” *Front. Nucl. Eng.*, **2**, 1214727 (2023).
2. S. A. WALKER, M. E. TANO, A. ABOU-JAOUDE, and P. BAJPAI, “Multiphysics Chemical Species Transport Framework for Molten Salt Reactor Analysis,” *Eur. Phys. J. Nucl. Sci. Tech.*, Topical Issue on modeling breakthroughs for Advanced Nuclear Reactors, [Manuscript in Preparation] (2024).

Sections 2 and 3 will provide additional background information on the importance of chemical species transport in MSRs. These sections will also detail the multiphysics framework approach developed by this work and summarize the specific proof-of-concept applications of the framework that were modeled this FY. Sections 4–6 cover a broad spectrum of results focusing on chemical-species transport to an off-gas system and corrosion with and without active-chemistry control that were obtained through the development of the multiphysics framework. Finally, Section 7 discusses the primary conclusions of the work accomplished in FY-23 and focuses on future work and synergistic activities planned for FY-24. Section 8 summarizes this milestone.

## 2. IMPORTANCE OF CHEMICAL-SPECIES TRANSPORT IN MSRS<sup>a</sup>

As mentioned earlier, chemical-species transport is an important driving factor that affects the multiphysics behavior of MSRs during both normal-operation and accident-transient scenarios. To better understand this effect, it is important to discuss the relationship between chemical-species transport and the redox potential of the fuel salt.

### 2.1. Definition of the Redox Potential in Relation to the Fluorine or Chlorine Potential

The chemical behavior of molten salts is largely dependent on the redox potential of the fuel salt. The baseline potential for measuring the redox potential can be stated in reference to the chemical potential of the base ion of the ionic salt (i.e., fluorine or chlorine chemical potential) as seen in Equation (2.1) [5]. Here,  $R$  is the ideal gas constant in units of [J/(mol · °K)],  $T$  is the temperature of salt in °K, and  $p_{F_2}$  is the unitless partial pressure of fluorine gas (i.e.,  $F_{2(g)}$ ) in the molten salt; thus, the units of  $\Delta\bar{G}_{F_2}$  are most commonly [J/mol] or [kcal/mol].

$$\Delta\bar{G}_{F_2} \equiv RT \ln p_{F_2} \quad (2.1)$$

Additionally, the fluorine chemical potential can be related to the electrochemical potential  $E$  of the molten salt via Equation (2.2) [6].

$$\Delta\bar{G}_{F_2} \equiv RT \ln p_{F_2} = -nFE \quad (2.2)$$

Here,  $F=96,485$  [C/mol] is the Faraday constant, representing the amount of charge per mol of electrons, and  $n$  is the number of electrons transferred in the reaction where the standard state reaction is given as Equation (2.3) [7]. The reference potential for the standard state half-cell reaction is set at 0 V as shown in Equation (2.3).



Essentially the fluorine chemical potential is a measurement of how strongly the fluorine in a system can oxidize or dissolve other elements in the system. In the remainder of this article, the electrochemical redox potential and the fluorine or chlorine chemical potential of the fuel salt will be used interchangeably with the understanding that the potential to which we refer is linked to the base ion in the modeled salt system.

### 2.2. Chemical-Species Transport and Fuel-Salt Redox Potential

The fluorine or chlorine potential of fluoride and chloride salts, respectively, is heavily influenced by the chemical composition of cations present. These make up the ionic molten salt [7]. During normal reactor operations, the chemical composition of the fuel salt will gradually change as it undergoes nuclear fission, causing fissionable heavy metals to be replaced by soluble or insoluble fission products. Additionally, non-fission transmutation of the fuel salt through capture reactions and radioactive decay will also occur, altering the concentrations of actinides (e.g., neptunium, plutonium) as well as FPs in the fuel salt. The fuel salt chemical composition can also be altered by chemical species extracted from the fuel salt via off-gassing of volatile species or by additions of metallic nuclides to the fuel salt in the form of soluble species that are then dissolved in the fuel salt.

---

a Portions of this Section previously appeared as: S. A. Walker, M. E. Tano, A. Abou-Jaoude, and O. Calvin, "Depletion-driven thermochemistry of molten salt reactors: review, method, and analysis," *Front. Nucl. Eng.*, **2**, 1214727 (2023) [2].

These changes in chemical composition due to depletion directly alter the fuel salt’s redox potential. This, in turn, determines how the fuel and fission products behave in solution, as well as how structural materials interact with the salt via corrosion mechanisms. Therefore, depletion-driven thermochemistry is a critical force in determining reactor behavior during normal-operation and accident scenarios. This includes long-term corrosion effects on key reactor components and the evolution of radionuclide source terms (dictated by nuclide vapor pressures) in the molten salt over reactor lifetimes. Ultimately, this multiphysics effect is an important consideration for future MSR reactor design, licensing, and operation.

## 2.3. Chemical Species Transport in the Molten Salt Reactor Experiment

To better understand chemical-species transport, it is helpful to review the first comprehensive operational example of an MSR—the Molten Salt Reactor Experiment (MSRE). The MSRE was a fluoride salt reactor that operated in Oak Ridge National Laboratory (ORNL) in the 1960s. It maintained operations for 11,500 equivalent full-power hours using both <sup>235</sup>U- and <sup>233</sup>U-based fuel dissolved in the molten salt [8]. The reactor was considered a successful proof of concept of liquid-fuel technology, showcasing the benefits of such a design as well as identifying the remaining technical challenges that must be resolved by future research.

The implementation of chemistry control of the fuel salt was a critical aspect of reactor operations. It was anticipated that structural materials present in the Hastelloy-N alloy, used for the reactor vessel and piping, would reduce UF<sub>4</sub> to UF<sub>3</sub> to some limited extent, forming soluble corrosion products in the fuel salt, as seen in Equation (2.4), where the corrosion of chromium into the fuel salt is highlighted [9].



Therefore, the molten-salt system at thermodynamic equilibrium should be “poised” or buffered by the UF<sub>4</sub>-UF<sub>3</sub> redox couple, and a small amount of CrF<sub>2</sub> should be present. However, as UF<sub>4</sub> and UF<sub>3</sub> are consumed and transmuted during depletion, the total amounts and ratio of this redox couple can change. If they change significantly enough, the system could be increasingly poised or buffered by another redox couple.

In the case of the system shifting towards an oxidizing state where the UF<sub>4</sub>-to-UF<sub>3</sub> ratio is large or increasing, then the redox couple Cr<sub>(s)</sub>-CrF<sub>2</sub> becomes dominant and poises the system. This system would then be in an active state of corrosion, where thermodynamic equilibrium is dependent on the amount of Cr<sub>(s)</sub> that could be extracted from the structural surfaces in contact with the fuel salt. On the other hand, if the system shifts towards a reducing state where the UF<sub>4</sub>-to-UF<sub>3</sub> ratio is small or decreasing, then the redox couple UF<sub>3</sub>-U<sub>(s)</sub> would become dominant and poise the system. Under these conditions, uranium would solidify and precipitate out of the fuel salt due to a lack of fluorine potential.

### 2.3.1. Understanding Relative Redox Potentials of Reactions

To illustrate this point more clearly, a standard half-cell redox-potential table, calculated from the MSRE, is reproduced here as Table 2-1 [7]. This table lists the standard half-cell electrochemical redox potentials calculated in FLiBe salt in relation to the fluorine chemical potential where the standard half-cell potential is defined by Equation (2.3). It is important to note that these redox potentials shown in Table 2.1 are standard at 1000 K whereas traditional standard cell potentials by definition mean that the voltage is measured or calculated at 298 K, 1 atm, and 1 M or 1.0E<sup>-3</sup> mol/cm<sup>3</sup> solutions. Because these ionic melts would not be liquid at 298 K, the standard potentials are calculated at 1000 K instead, and the other standard states (i.e., pressure and chemical activity) remain the same.

The redox potential of a reaction not at standard states (i.e., redox potentials not calculated or measured at 1000 K, 1 atm, and  $1.0E^{-3}$  mol/cm<sup>3</sup> solutions) can be calculated by the Nernst equation, shown in Equation (2.5) [10]. Here  $E$  is the redox potential of the reaction at non-standard states,  $E^O$  is the standard cell potential of the complete reaction (i.e., the addition of two half-cell reactions shown in Table 2-1), and  $Q$  is the reaction quotient, which is a ratio of the relative chemical activities of the products to the reactants in the reaction.

$$E = E^O - \frac{RT}{nF} \ln Q \quad (2.5)$$

Building upon this point then, the standard redox-potential half-cell reactions in Table 2-1 show the relative likelihood of different reactions happening at different redox potentials with the implicit notion that the chemical activity of the elements being dissolved in the FLiBe salt are all equal to  $1.0E^{-3}$  mol/cm<sup>3</sup>. However, it should be stressed that the redox potential of reactions depend heavily on the chemical activities of the products and reactants of the reactions as seen in the  $Q$  term of Equation (2.5). Therefore, the relative redox potentials of reactions in a real MSR system made up of base-salt elements, fuel, fission products, and corrosion products is not as linear as the table may suggest. A plethora of reactions, shown (and more not shown) in Table 2-1, will be at various  $Q$  values for a given redox potential, depending on the chemical activities of the elements in the fuel salt.

Table 2-1. Calculated electrode potential in LiF-LiF-0.33 BeF<sub>2</sub> (1000 K) (reformatted from [7]).

Half Cell Reactions	$E^O$ (1000 [K]), (V)
$Li^+ + e^- \leftrightarrow Li_{(s)}$	-5.412
$La^{3+} + 3e^- \leftrightarrow La_{(s)}$	-5.081
$Ce^{3+} + 3e^- \leftrightarrow Ce_{(s)}$	-5.011
$Sm^{3+} + 3e^- \leftrightarrow Sm_{(s)}$	-4.881
$Th^{4+} + 4e^- \leftrightarrow Th_{(s)}$	-4.601
$Be^{2+} + 2e^- \leftrightarrow Be_{(s)}$	-4.592
$U^{3+} + 3e^- \leftrightarrow U_{(s)}$	-4.281
$U^{4+} + 4e^- \leftrightarrow U_{(s)}$	-4.190
$Zr^{4+} + e^- \leftrightarrow Zr_{(s)}$	-4.187
$U^{4+} + e^- \leftrightarrow U^{3+}$	-3.915
$Cr^{2+} + 2e^- \leftrightarrow Cr_{(s)}$	-3.261
$Fe^{2+} + 2e^- \leftrightarrow Fe_{(s)}$	-2.882
$HF_{(g)} + e^- \leftrightarrow F^- + \frac{1}{2}H_2(g)$	-2.871
$Ni^{2+} + 2e^- \leftrightarrow Ni_{(s)}$	-2.398
$\frac{1}{2}F_2(g) + e^- \leftrightarrow F^-$	0.0

As can be at the top of Table 2-1, the most-stable ions are the base-salt ions  $Li^+$  and  $Be^{2+}$  in addition to a host of rare-earth fission-product ions. The low redox-potential values of these reactions means that it takes a very limited fluorine potential to sufficiently dissolve these elements in the molten salt or that they readily form ion pairs with fluorine whereas, for more-positive redox-potential values, a larger fluorine chemical potential is required to dissolve these elements in the molten salt.



As discussed earlier, if the redox potential is poised by the  $U^{4+}$ - $U^{3+}$  ( $UF_4$ - $UF_3$ ) pair in the salt, as seen in Equation (2.4) (i.e., their chemical activities are thermochemically dominant in dictating the fluorine chemical potential), then the redox potential of the fuel salt at thermochemical equilibrium is held somewhere below -3.915 V. Therefore, more positive redox potential reactions further down Table 2-1 will not be significant (i.e., corrosion of  $Cr_{(s)}$ ,  $Fe_{(s)}$ , and  $Ni_{(s)}$  is controlled).

As uranium fissions, however, the relative chemical activities of the  $U^{4+}$ - $U^{3+}$  buffer pair is sufficiently altered, and the redox potential shifts towards the next thermochemically favorable buffer pair. The resulting two fission products generated in the fuel salt have an aggregated electrochemical potential that is more positive than the single uranium atom they replace; hence, the electrochemical potential of the system increases or becomes more oxidizing [11]. Moving down Table 2-1, if the chemical activity of  $Cr_{(s)}$  in the structural-material alloy in thermodynamic equilibrium with the salt is large enough, then the  $Cr_{(s)}$ - $Cr^{2+}$  will become the dominant redox-potential buffer pair, and the redox potential of the fuel salt will be held somewhere below to -3.261 V.

### 2.3.2. Changing Redox Potential in the MSRE

If fluorine has a less-negative chemical potential, then  $UF_4$  is overly dominant, and the formation of corrosion products will occur as seen in Equation (2.4) when the  $Cr_{(s)}$ - $Cr^{2+}$  buffer becomes dominant. If the fluorine potential continues to increase, then in addition to significant corrosion of structural materials leaching  $Cr_{(s)}$ ,  $Fe_{(s)}$ , and  $Ni_{(s)}$  into the fuel salt,  $UF_{5(g)}$  and  $UF_{6(g)}$  (not shown in Table 2-1) will eventually form as well.

The chemical-activity ratio of  $UF_4$  to  $UF_3$  can be used to understand the current redox potential of the fuel salt and was, therefore, the primary method used to determine the chemical state of the fuel salt during the MSRE, as seen in Figure 2-1 [12]. Ideally, the fluorine potential of the fuel salt would be actively controlled and held steady during reactor operation so that corrosion rates and fission-product behavior in the fuel salt would be predictable.

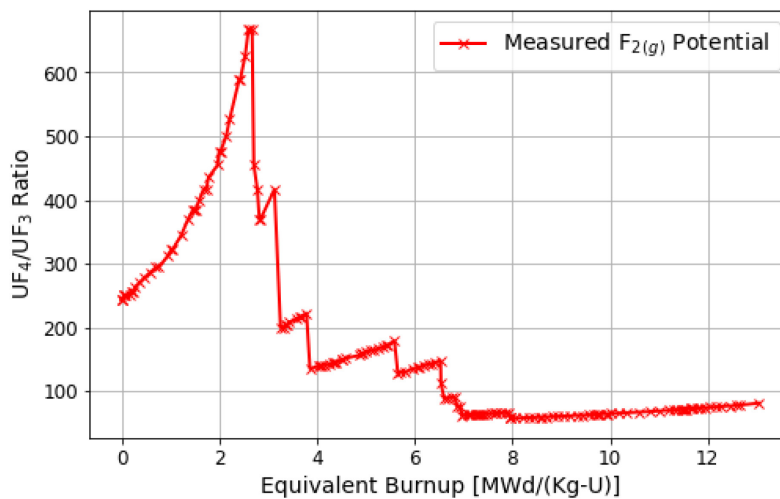


Figure 2-1.  $UF_4$  to  $UF_3$  ratio during the  $^{235}U$  MSRE runs (reformatted from [12]).

However, as seen in Figure 2-1, the redox potential of the fuel-salt during the MSRE did not remain steady during the entire reactor operation [12]. During the first ~2000 full power hours (or ~2.5 MWd/Kg-U burnup) of the MSRE, the  $UF_4$ : $UF_3$  ratio rose without active chemistry control. This experimental data showcases how, as depletion occurs, the chemical environment of the fuel salt becomes more oxidizing where the fluorine chemical potential increases over time.

Another way to understand this process is that fuel salt develops a cationic charge deficiency due to depletion as dissolved uranium metal is consumed and the fission products that are generated are not as thermochemically stable in fluorides as the original uranium fuel (i.e., noble-metal and noble-gas fission products Mo, Tc, Xe, Kr) and do not form ion pairs with fluorine (i.e., their cationic charge = 0). To fill this cationic charge deficiency, or to satisfy the increased fluorine chemical potential, the chemical reaction in Equation (2.4) comes into effect to form a new thermochemical equilibrium with a significant amount of corrosion products that have leached into the fuel salt from structural materials in direct contact with the fuel salt.

To limit corrosion, another option to reduce the redox potential of the fuel salt is to replace the cationic charge deficiency that develops due to depletion with a more thermochemically stable metal higher up Figure 2-1 (e.g., more U or Be) as seen in Equation (2.6). In this case, the chemical activity of the  $\text{Be}_{(s)}\text{-Be}^{2+}$  buffer ratio becomes thermochemically dominant and dictates the fluorine potential.



This is exactly what is occurring in Figure 2-1 when the  $\text{UF}_4\text{:UF}_3$  ratio sharply decreases; the MSRE fuel salt is being actively reduced through the dissolution of Be into the fuel salt. This process was monitored by taking a fuel-salt sample at an interval of several days to determine the  $\text{UF}_4\text{:UF}_3$  ratio, before the beryllium rod was immersed into the fuel salt for a period of a few hours [12].

### 3. MULTIPHYSICS-FRAMEWORK APPROACH

As described earlier, the key thrust of this work was to couple various NEAMS codes, based upon the Multiphysics Object Oriented Simulation Environment (MOOSE) framework [13], and develop a comprehensive framework for multiphysics and multiscale analysis of chemical-species transport in MSRs. This framework was then used to model the volatilization, transport, and extraction of chemical species throughout burnup in MSR systems and to model corrosion-product formation and active-chemistry control.

The workflow for a multiphysics approach to model chemical-species transport will require, at each time step, information on the chemical equilibrium, thermal hydraulics, and mass-transfer/reaction kinetics occurring in the reactor system. NEAMS codes, built upon or wrapped into the MOOSE framework, are ideally suited for this multiphysics and multiscale problem.

Specifically, tools like Griffin [14] can be leveraged for neutronics and depletion. Pronghorn [15], the Systems Analysis Module (SAM) [16], or the open-source Thermal Hydraulics Module (THM) in MOOSE can be employed for thermal-hydraulics. Last, Thermochemica [17], Mole [18], or the open-source Chemical Reactions Module (CRM) in MOOSE can be used for mass-transfer/reaction kinetics and chemical equilibrium calculations. The coupled-NEAMS workflow to solve this multiphysics problem is shown in Figure 3-1.

It is worth noting that this approach was initially proposed by [18] and partially executed in [19], but it is slightly modified here to prioritize NEAMS based codes, specifically ones that are easily coupled via the MOOSE framework and provide multiscale fidelity to match the physics requirements of the problem.

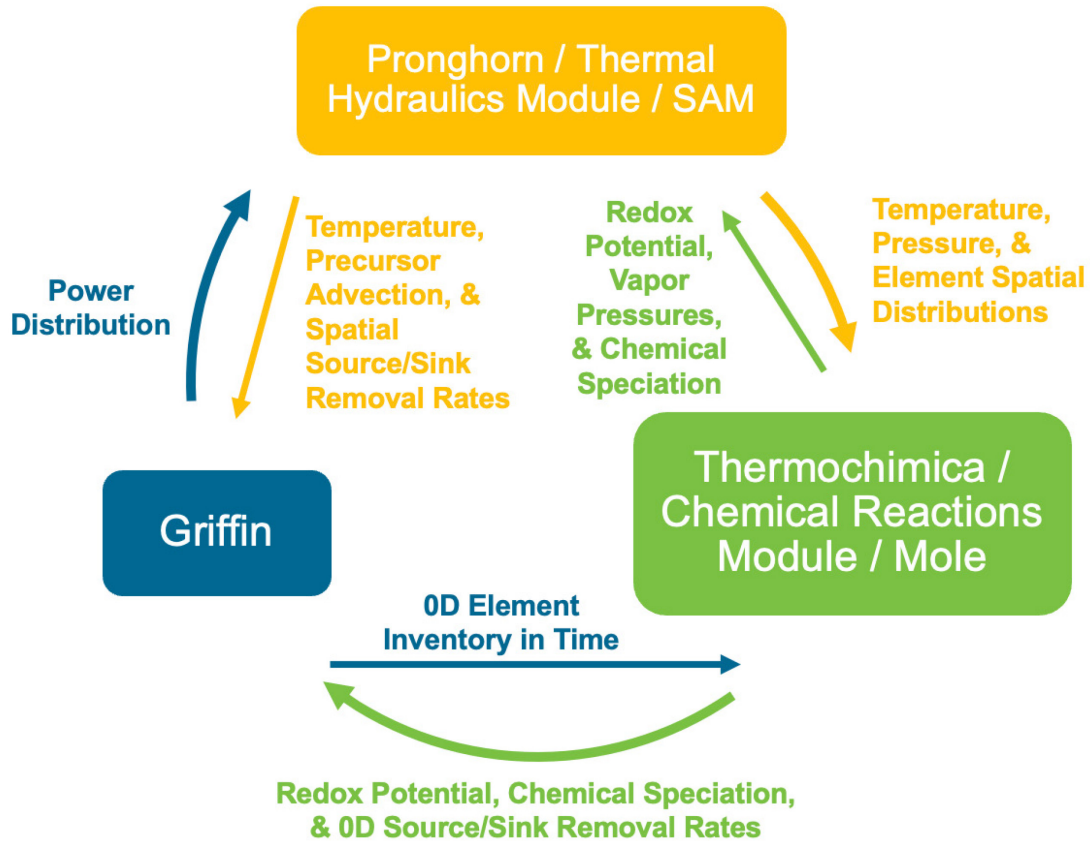


Figure 3-1. NEAMS based multiphysics and multiscale framework for chemical species transport in MSR systems.

As part of this FY’s work, three primary steps in setting up the framework and executing this workflow for chemical-species transport in MSR systems were conducted. These steps directly correlate with the three primary codes listed in the workflow wheel and their coupling for multiphysics analysis: Griffin, Pronghorn, and Thermochemica within the MOOSE framework. The following steps accomplished this fiscal year are as follows:

1. **Depletion-driven thermochemistry (Griffin + Thermochemica):** 0D multi-region (reactor loop and off-gas system) depletion, with isotopic removal in Griffin informed by chemical speciation at each time step via chemical-equilibrium calculations done in Thermochemica.
2. **Spatially resolved thermochemistry (Pronghorn + Thermochemica):** Spatially resolved equilibrium chemistry calculations by Thermochemica given temperature, pressure, and element distributions calculated by Pronghorn.
3. **Depletion-driven spatially resolved thermochemistry (Griffin + Pronghorn + Thermochemica):** Spatially resolved depletion and chemistry by superimposing long-lived and well-mixed (i.e., homogenous) nuclides and elements calculated by Griffin depletion and medium-lived nuclides with spatial dependence calculated by Pronghorn.

A detailed breakdown and the key findings of accomplishing these steps is provided in Sections 4–6 for Steps 1–3, respectively. Before continuing to these results sections, it is important to dig deeper into what task each NEAMS code performs and how it contributes to the multiphysics solution of the MSR system.

### 3.1. Griffin Depletion<sup>b</sup>

Griffin is a NEAMS tool used for multifidelity neutronics and fuel depletion. Recent efforts in FY-22 incorporated nuclide removal and multi-region microscopic depletion capability for modeling off-gas and other waste streams in MSR systems during burnup [20].

The depletion equation solved by Griffin, also known as the Bateman equations, track the nuclide number density of the fuel and resulting fission products, and incorporates fission, neutron transmutation, and radioactive decay as seen in Equation (3.1). Equation (3.1) has additional terms not traditionally seen in the Bateman equations, which represent sources and sinks from removal waste streams and from chemical reactions at interfaces.

$$\frac{dN_Z^A(t)}{dt} = \sum_{Z',A'=1}^M \left( \gamma_Z^A \sum_{g=1}^G \sigma_{f(Z',A'),g}(t) \phi_g(t) + \sum_{g=1}^G \sigma_{(Z',A') \rightarrow (Z,A),g}(t) \phi_g(t) + r_{(Z',A') \rightarrow (Z,A)} \lambda_{Z'}^{A'} \right) N_{Z'}^{A'}(t) - \lambda_Z^A N_Z^A(t) - \sum_{g=1}^G \sigma_{a(Z,A),g}(t) \phi_g(t) N_Z^A(t) - f_{chem,Z}^A(t) - f_{stream,Z}^A(t) \quad (3.1)$$

where

$N_{Z'}^{A'}(t)$  is the number density of other nuclides with atomic number  $Z'$  and mass number  $A'$ , which produce nuclide  $N_Z^A(t)$

$\gamma_Z^A$  is the fission yield of nuclide  $N_Z^A$  from  $N_{Z'}^{A'}(t)$

$\sigma_{f(Z',A'),g}(t)$  is the groupwise microscopic fission cross section of  $N_{Z'}^{A'}(t)$

$\phi_g(t)$  is the groupwise scalar neutron flux

$\sigma_{(Z',A') \rightarrow (Z,A),g}(t)$  is the groupwise microscopic transmutation cross section of  $N_{Z'}^{A'}(t)$  that produces  $N_Z^A(t)$

$r_{(Z',A') \rightarrow (Z,A)}$  is the branching ratio for radioactive decay

$\lambda_{Z'}^{A'}$  is the radioactive decay constant for  $N_{Z'}^{A'}(t)$

$\lambda_Z^A$  is the radioactive decay constant for  $N_Z^A(t)$

$\sigma_{a(Z,A),g}(t)$  is the groupwise absorption cross section for  $N_Z^A(t)$

$f_{chem,Z}^A(t)$  is a chemical reaction source at interfaces

$f_{stream,Z}^A(t)$  is a mass transfer removal source term for feed and waste streams.

One application of this code focuses on using the term  $f_{stream,Z}^A(t)$ , where nuclides will be withdrawn or added to the reactor system. This alters the ongoing depletion of the fuel and nuclide inventory. Altering the  $f_{stream,Z}^A(t)$  term, changes the chemical composition, and this will drive any observed thermochemical-equilibrium changes in the fuel salt. The form that  $f_{stream,Z}^A(t)$  takes is defined in Equation (3.2), a type of effective removal rate that depends on the existing amount of the nuclide in the fuel salt and a feed rate  $L$ , where  $L$  can be positive or negative for material additions or subtractions from the system.

$$f_{stream,Z}^A(t) = LN_Z^A(t) \quad (3.2)$$

---

<sup>b</sup> Portions of this subsection previously appeared as: S. A. Walker, M. E. Tano, A. Abou-Jaoude, and O. Calvin, "Depletion-driven thermochemistry of molten salt reactors: review, method, and analysis," *Front. Nucl. Eng.*, **2**, 1214727 (2023) [2].

### 3.2. Pronghorn Species Transport<sup>c</sup>

The coarse-mesh thermal-hydraulics code Pronghorn is the NEAMS mid-fidelity option for solving the Navier-Stokes equations in advanced-reactor cores [21]. In Sections 5 and 6, the molten-salt fast reactor (MSFR) model [22], taken from the Virtual Test Bed (VTB) [23], is used in several analyses that involve Pronghorn. Therefore, Pronghorn will be introduced in the context of the MSFR model [22]. Using many assumptions to simplify the Navier-Stokes equations, the conservation of mass, momentum, and energy equations at steady state solved by Pronghorn are listed in Equations (3.3–3.5) [22]:

$$\nabla \cdot \vec{u} = 0, \quad (3.3)$$

$$\nabla \cdot \rho \vec{u} u_x + \frac{\partial}{\partial x} P - (\mu + \mu_t) \nabla^2 u_x - f_{fric,x} = 0, \quad (3.4)$$

$$\nabla \cdot T \vec{u} - \nabla \cdot \epsilon_q \nabla T - \frac{1}{\rho c_p} Q_q = 0, \quad (3.5)$$

where

$\vec{u}$  is velocity

$u_x$  is the velocity component in the x direction

$\rho$  is the density

$P$  is the pressure

$\mu$  and  $\mu_t$  are the viscosity and turbulent viscosity, respectively

$f_{fric,x}$  is the friction force in the x direction

$T$  is the temperature

$\epsilon_q$  is the eddy diffusivity for heat

$c_p$  is the heat capacity

$Q_q$  is the volumetric heat generation rate of the molten salt fluid respectively.

Solving these equations gives solutions for the velocity, pressure, and temperature field in the MSFR.

In addition to the temperature and pressure fields, the concentration distribution of chemical species is a key parameter for thermochemistry. Equation (3.6) is the general chemical species-transport equation implemented in Pronghorn:

$$\nabla \cdot (\vec{u} c_i) - \nabla \cdot \epsilon_c \nabla c_i - \lambda_i c_i = \gamma_i f, \quad (3.6)$$

where

$c_i$ ,  $\lambda_i$ , and  $\gamma_i$  are the concentration, decay constant, and fission yield for chemical species  $i$ , respectively

$\epsilon_c$  is the eddy diffusivity

$f$  is the fission rate.

---

<sup>c</sup> Portions of this subsection will appear as: S. A. WALKER, P. BAJPAI, D. SCHWEN, M. E. TANO, and A. ABOU-JAOUDE, "Spatially Resolved Thermochemistry with Chemical Species Tracking in Molten Salt Reactors," *Trans. Am. Nucl. Soc. (Winter Meeting 2023)*, Washington D.C., November 12–15, 2023, [Summary submitted for publication] (2023).

In this instance, nuclides can be tracked explicitly and then summed into elemental-composition distributions for thermochemical calculations in Thermochemica. Here, steady-state distributions for medium-lived nuclides (i.e., nuclides with a residence time in the reactor on the order of the circulation time of the system) are calculated in Pronghorn for spatially resolved thermochemistry.

### 3.3. Thermochemica Chemical Equilibrium<sup>d</sup>

The thermochemistry library Thermochemica [24] was developed to couple with multiphysics codes, and it was recently integrated into the CRM of MOOSE [25]. Using the Gibbs energy-minimization method, Thermochemica can calculate the stable-phase assemblage of a system given its temperature, pressure, and composition. It can also provide various material properties and boundary conditions, such as element potentials. In MSR simulations, Thermochemica can help in mass accountancy because the dissolved fissile material flows in the entire loop and interacts with several components. Furthermore, the addition and removal of fission products also changes salt chemistry and can be of safety concern due to corrosion, off-gassing, etc. Thermochemica minimizes the integral Gibbs energy of the system, which is given as Equation (3.7):

$$G = \sum_{\phi=1}^{\Phi} n_{\phi} \sum_{i=1}^{N_{\phi}} x_i \mu_i, \quad (3.7)$$

where,

$G$  is the Gibbs energy of the system

$n_{\phi}$  is the number of moles of phase  $\phi$  in the system

$x_i$  and  $\mu_i$  are the mole fraction and chemical potential of species  $i$  of phase  $\phi$ .

The above equation results in a non-linear, non-convex Gibbs-energy function, and Thermochemica aims to identify a unique combination of the molar amounts of phases and the mole fractions of the species such that the Gibbs energy of the system is at a global minimum. This is subject to the mass-balance constraint, which is given as Equation (3.8):

$$b_j = \sum_{\phi=1}^{\Phi} n_{\phi} \sum_{i=1}^{N_{\phi}} x_i \nu_{ij}, \quad (3.8)$$

where,  $b_j$  represents the molar amount of element  $j$  in the system and  $\nu_{ij}$  denotes the stoichiometry of element  $j$  in species  $i$ . Also, the Gibbs phase rule must be respected. It imposes a constraint on the degree of freedom of the system as follows in Equation (3.9):

$$F = C - \Phi, \text{ where } F \geq 0. \quad (3.9)$$

In Equation (3.9),  $C$  denotes the number of elements in the system, and  $\Phi$  denotes the number of phases. For most phases, the Gibbs energy is composed of a reference, an ideal mixing term, and an excess mixing contribution. For molten salts, the modified quasichemical model in Quadruplet Approximation [26] is often used, and Thermochemica has the mixing models required for such systems. A thermodynamic database is required by Thermochemica and, while it supports any database in the ChemSage format, the Molten Salt Thermodynamic Database: Thermochemical (MSTDB-TC), V2.0 [27] was used because it has many validated and quality-controlled thermodynamic treatments.

---

<sup>d</sup> Portions of this subsection will appear as: S. A. WALKER, P. BAJPAI, D. SCHWEN, M. E. TANO, and A. ABOU-JAOUDE, "Spatially Resolved Thermochemistry with Chemical Species Tracking in Molten Salt Reactors," *Trans. Am. Nucl. Soc. (Winter Meeting 2023)*, Washington D.C., November 12–15, 2023, [Summary submitted for publication] (2023) [4].

### 3.4. Selected Applications of Chemical Species Transport in MSRs

As mentioned in Table 1-1, many possible applications of this new framework apply to MSR modeling and simulation. This section details two of the applications analyzed during the development of the framework: chemical speciation for off-gas analysis and corrosion with and without active chemistry control.

#### 3.4.1. Chemical Speciation and Off-Gas Analysis

The first application of the framework was the chemical speciation and transport to an off-gas system, as shown in Figure 3-2. This is a natural application because the changing thermochemical state of the fuel salt due to depletion is critical in determining nuclide chemical behavior and volatilization. Here  $\text{CsI}_{(l)}$  and a small amount of  $\text{CsI}_{(g)}$  are formed and can be extracted to the off-gas system depending on reactor design and specifications.

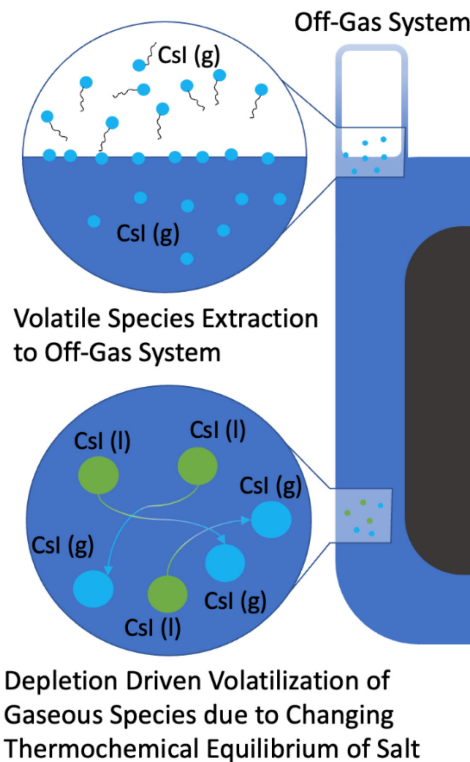


Figure 3-2. Depletion-driven volatilization of gaseous species to off-gas system.

Determining the rate of volatile-nuclide extraction to an off-gas system involves depletion (Griffin), chemical speciation (Thermochemica), and species transport (Pronghorn). Understanding the amounts and types of material being extracted to an off-gas system can directly impact the possible applications listed in Table 1-1. Therefore, a depletion-driven spatially resolved thermochemical-modeling approach is necessary to determine the volatilization of nuclide species from an MSR core to an off-gas system. This model affects a host of multiphysics analyses in Table 1-1, and these analyses can be used to inform off-gas system requirements and future experimental reactor-demonstration designs.

### 3.4.2. Corrosion and Active Chemistry Control Analysis

As highlighted in Section 1, a critical aspect to chemical-species transport is the changing fluorine or chlorine chemical potential of the system, also known as the redox potential of the fuel salt. In a depletion-driven process, the changing redox potential of the fuel salt, can affect corrosion and must be actively controlled, as seen in Figure 3-3. Here, corrosion of structural materials (i.e., Cr and Fe) occurs due to changes in the temperature and fluorine potential in the reactor system. Active-chemistry-control methods, including reducing metal additions (i.e., a Be rod) are a key aspect to achieve fuel-salt chemistry control.

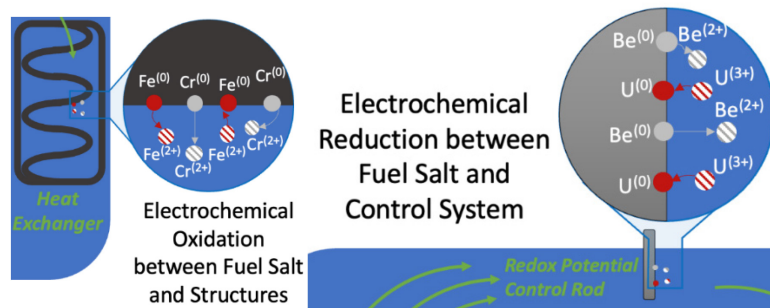


Figure 3-3. Depletion-driven corrosion of structural materials and active chemistry control.

The changing thermochemistry due to corrosion, with and without control, also effects the volatility of chemical species in the system and the amounts of material being extracted to the off-gas system. Similarly, corrosion and active-chemistry control can have an important effect on the other analyses listed in Table 1-1. Therefore, a depletion-driven, spatially resolved thermochemistry analysis of corrosion with and without active-chemistry control is not only important for determining reactor-component lifetimes, but is also essential to model, predict, and ultimately control MSR systems.

The next sections showcase the coupling steps and the resulting new modeling and simulation analyses that were conducting during the formation of the framework. Specifically, the following section looks at the primary driving factor for chemical speciation and corrosion in MSRs—depletion driven thermochemistry.



## 4. DEPLETION-DRIVEN THERMOCHEMISTRY (GRIFFIN + THERMOCHIMICA)

### SECTION RELATED PUBLICATIONS

The work focused on this coupling and analysis resulted in three publications listed below.

#### Conference Publications:

1. S. A. WALKER, M. E. TANO, and A. ABOU-JAOUDE, “Leveraging Coupled Thermochemical Depletion Capabilities to Evaluate Off Gas and Source Term Characterization in Molten Salt Reactor Systems,” *Proc. Intl. Cong. Adv. Nucl. Pow. Plnts. (ICAPP 2023)*, Gyeongju, South Korea, April 23–27, 2023, Paper #1334 (2023).
2. S. A. WALKER, M. E. TANO, and A. ABOU-JAOUDE, “A Coupled Griffin and Thermochemica Method for Redox Potential Control and Off-Gas Analysis During Depletion in Molten Salt Reactors,” *Proc. Intl. Conf. Math. Comp. Mthds. Nucl. Sci. Eng. (M&C 2023)*, Niagara Falls, Ontario, Canada, August 13–17, 2023, Accepted for Publication (2023).

#### Journal Publications:

1. S. A. WALKER, M. E. TANO, A. ABOU-JAOUDE, and O. CALVIN, “Depletion-driven thermochemistry of molten salt reactors: review, method, and analysis,” *Front. Nucl. Eng.*, **2**, 1214727 (2023).

One of the largest challenges in predicting MSR multiphysics behavior lies in understanding how the chemistry of fuel-bearing molten salts will change over the reactor lifetime as the MSR fuel salt undergoes depletion and how, in turn, chemical changes in the molten salt will affect the isotopic evolution of the reactor. This multiphysics coupling is coined by this work as “depletion-driven thermochemistry,” and the code coupling required for this analysis is shown in Figure 4-1. It is defined as neutronic-driven changes in fuel-salt chemistry over time due to the process of depletion. Here, thermochemistry refers to the chemical compounds and chemical state of the molten-salt ionic liquid, while depletion refers to the processes of fission, decay, and neutron capture that deplete the fissionable material and create an extensive inventory of fission and activation products in the fuel salt.

This section presents some key results obtained using the multiphysics-coupled, depletion-driven thermochemistry scheme detailed in the previous section. First, the specifications of the generic zero-dimensional fluoride and chloride MSRs are defined. The following subsections detail the changing fluorine and chlorine potential of the systems as they undergo depletion. Vapor pressures for chemical species in both systems are also calculated throughout burnup. Finally, active redox-chemistry control is modeled, and the resultant changing thermochemical equilibrium of the fuel salt is calculated.

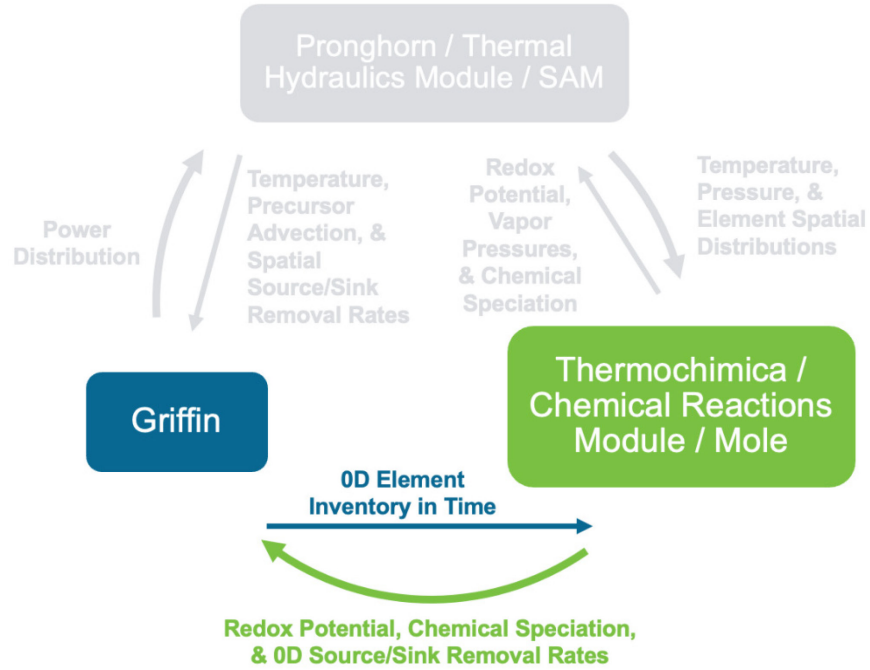


Figure 4-1. Depletion-driven thermochemistry code coupling.

Table 4-1 identifies the specifications used in the depletion-driven thermochemical analysis of these two generic reactor types. The fluoride-salt composition was selected to be close to that of the MSRE fuel salt, with the notable exception that the Zr component is missing as mentioned earlier [12]. Instead, it is very similar to pure FLiBe (2LiF-BeF<sub>2</sub>) salt with the replacement of some beryllium with uranium fuel. Additionally, the <sup>235</sup>U enrichment of the system was set to 33.3% to match the MSRE fuel salt.

Table 4-1. Generic reactor specifications.

Specifications	Fluoride Reactor	Chloride Reactor
Initial Salt Composition [mol %]	LiF [66.4]-BeF <sub>2</sub> [32.7]-UF <sub>4</sub> [0.9]	NaCl [66.7]-UCl <sub>3</sub> [33.3]
Salt Density [g/cm <sup>3</sup> ]	1.94	3.13
<sup>235</sup> U Enrichment [%]	33.3	33.3
Temperature [K]	936.0	936.0
Pressure [atm]	1.34	1.34
Power Density [kW/cm <sup>3</sup> ]	0.01	0.01

The chloride-salt composition, on the other hand, is a chloride-eutectic fuel salt originally proposed for fast chloride breeder reactors [28]. Simply put, this is molten table salt mixed with some uranium fuel. Both the power densities and uranium enrichments are set equal so that the depletion histories can be compared between the two fuel-salt systems (i.e., the amount of uranium fuel consumed in both reactors is the same).

Due to the thermochemical-data limitations discussed in the previous section, a low burnup of 2.87 MWd/Kg-U is chosen for both reactors. To simplify the analyses, a constant scalar neutron flux is chosen, and one condensed energy group is used to evaluate the mid-burnup micro-cross-sections of nuclides in the reactor, as seen in [1,20] for both fluoride and chloride systems. Here the Monte Carlo code SERPENT-2 is used to generate the micro-cross-sections and to collapse the neutron flux into a single energy for both generic reactor systems [20,29].

## 4.1. Zero-Dimensional Chemical Speciation and Off-Gas Analysis<sup>e</sup>

This section presents some key results obtained using the multiphysics-coupled, depletion-driven thermochemistry scheme detailed in the previous subsection. The following subsections detail the changing fluorine and chlorine potential of the systems as they undergo depletion. Vapor pressures for chemical species in both systems are also calculated throughout burnup. Note that these analyses are limited in accuracy due to the lack of incorporation of spatial advection. Nevertheless, these zero-dimensional evaluations provide a useful guide to overall behaviors of the system and test some of the important mechanisms in the codes.

### 4.1.1. Fluoride Fuel Salt Analysis

The results of the multiphysics depletion-driven thermochemistry analysis of a fluoride fuel salt using the MSTDB-TC V2.0 during a 2.87 MWd/Kg-U burnup and 60 days of operation are presented below. Figure 4-2 showcases the change in fluorine potential and its associated redox potential, where Equation (2.3) sets the standard half-cell potential.

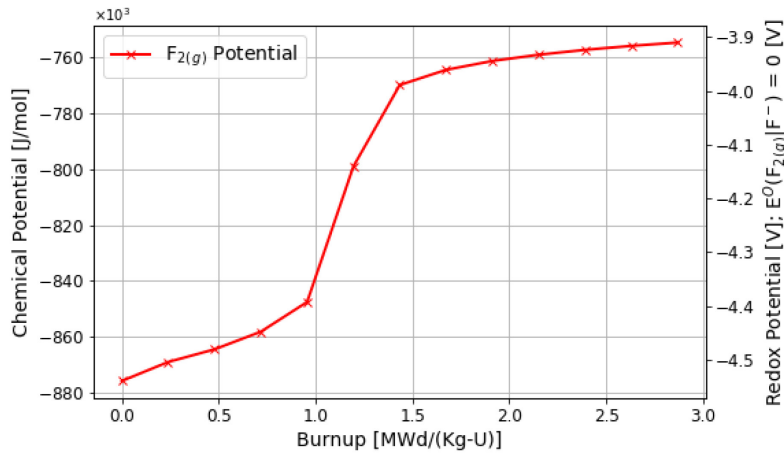


Figure 4-2. Change in fluorine potential over 60 days or 2.87 MWd/Kg-U burnup.

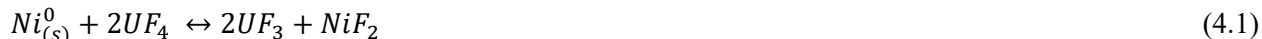
Here, the fluorine potential is steadily increasing over the first 1.0 MWd/Kg-U of burnup. This indicates that the fuel salt is becoming more oxidizing, which is the expected outcome of depletion—as observed in Figure 2-1 for the MSRE—where the  $UF_4/UF_3$  measurement of the redox potential is increasing. Although this analysis is not meant to be a direct comparison with the MSRE because the base MSRE fuel salt is not currently available in the MSTDB-TC V2.0, the redox potential increases more rapidly during the first 1 MWd/Kg-U of burnup than in the MSRE in Figure 2-1. This is especially true when the fluorine potential rapidly increases between 1.0 and 1.5 MWd/Kg-U of burnup. The results therefore indicate that the current MSTDB-TC V2.0 overestimates the depletion-driven evolution of the fluorine potential due to a lack of some important reducing fission products (e.g., Zr) for the fluoride fuel-salt system.

The apparent step change in fluorine potential observed from 1.0 to 1.5 MWd/Kg-U of burnup is related to a significant shift in the chemical activity of redox buffers, as discussed in Section 1. From 0.0 to 1.0 MWd/Kg-U of burnup, the fluorine potential is controlled by the  $UF_4/UF_3$  redox buffer pair. However, the chemical activity of  $UF_3$  greatly decreases as a cationic charge deficiency builds up due to

<sup>e</sup> Portions of this subsection previously appeared as: S. A. WALKER, M. E. TANO, A. ABOU-JAOUDE, and O. CALVIN, “Depletion-driven thermochemistry of molten salt reactors: review, method, and analysis,” *Front. Nucl. Eng.*, 2, 1214727 (2023) [2].

depletion. The  $UF_3$  is forced to shift towards  $UF_4$ , as seen in Equation (2.4). Eventually,  $UF_3$  is depleted, and the redox buffer will shift to the chemical activity ratio of  $Cr_{(s)}$  to  $Cr^{2+}$ .

However, in this analysis using the MSTDB-TC V2.0, corrosion and structural products Cr and Fe are not currently available, so the support structure in thermodynamic equilibrium with fuel salt available to be modeled in this analysis is pure  $Ni_{(s)}$ , with a chemical activity of 1.0 because there is no alloy. Therefore, the redox potential this analysis shifts from being dictated by the chemical activity ratio of  $UF_4:UF_3$  to the new redox buffer  $Ni_{(s)}$  to  $Ni^{2+}$  in, as seen in Equation (4.1).



This shift in redox-potential buffers can occur so rapidly in the fluoride fuel-salt composition chosen because the relative chemical activity of uranium is very small in the base fuel salt, as seen in Table 4-1 (i.e., 0.9 mol%). The missing chemical activities of key fission products may also be accentuated by the small amount of U contained in the fluoride fuel-salt system when compared to the chloride fuel-salt system analyzed in the following subsection. From 1.5 MWd/Kg-U of burnup onwards, the  $Ni_{(s)}-Ni^{2+}$  redox buffer poises the system, and the fluoride fuel salt is in a state of active corrosion, where  $NiF_2$  attempts to replace the cationic charge deficiency generated through depletion (i.e., it tries to take up the excess fluorine potential generated through the generation of less thermochemically stable fission products).

While this is a technical basis for the fluoride fuel-salt system, given the current thermochemical database, it is not necessarily representative of a real MSR system where the structural material is an alloy instead of pure  $Ni_{(s)}$ . As seen in Table 2-1 and Equation (2.4), a more-physical scenario would be the oxidation of  $Cr_{(s)}$  from the alloy materials into the fuel salt [30]. Therefore, the redox potential calculated here is similarly too high due to missing thermochemical data for Cr and Fe in fluoride salts. It should be lower, being controlled by the  $Cr_{(s)}-Cr^{2+}$  buffer instead. Ongoing development of the MSTDB-TC will likely rectify this issue in the near term [31]. The addition of  $ZrF_4$  (a base component of the MSRE fuel salt) and corrosion products  $CrF_2$  and  $FeF_2$  will enable the benchmarking of this multiphysics depletion-driven thermochemistry capability against the  $UF_4/UF_3$  data observed during the MSRE [12].

The results for vapor pressures in the fluoride fuel salt without active redox control are shown in Figure 4-3. Here, the highest vapor pressures are of the base-salt constituents (i.e., F, Li, Be) except for U. This is because these elements have the highest partial pressures in the system. The general trend for vapor pressures of minor fission- and transmutation-product elements is that they increase as their chemical activity builds up in the fluoride fuel salt. One key item of note for accident source-term analysis is that the vapor pressure of iodine in fluoride fuel salts significantly increases when the fluorine potential increases corresponding to Figure 4-2.

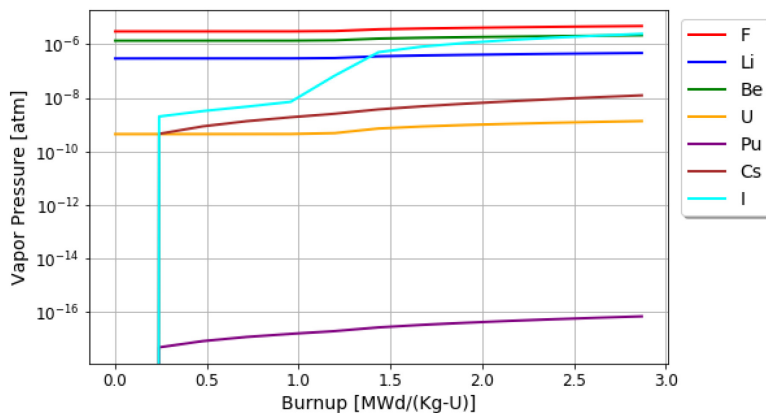


Figure 4-3. Changes in element vapor pressures in the fluoride fuel salt over 60 days or 2.87 MWd/Kg-U burnup.

### 4.1.2. Chloride Fuel Salt Analysis

The results of the multiphysics depletion-driven thermochemistry analysis of a chloride fuel salt using the MSTDB-TC V2.0 during a 2.87 MWd/Kg-U burnup and 60 days of operation are presented below. Figure 4-4 showcases the change in chlorine potential and its associated redox potential where the standard half-cell potential is defined by Equation (4.2).

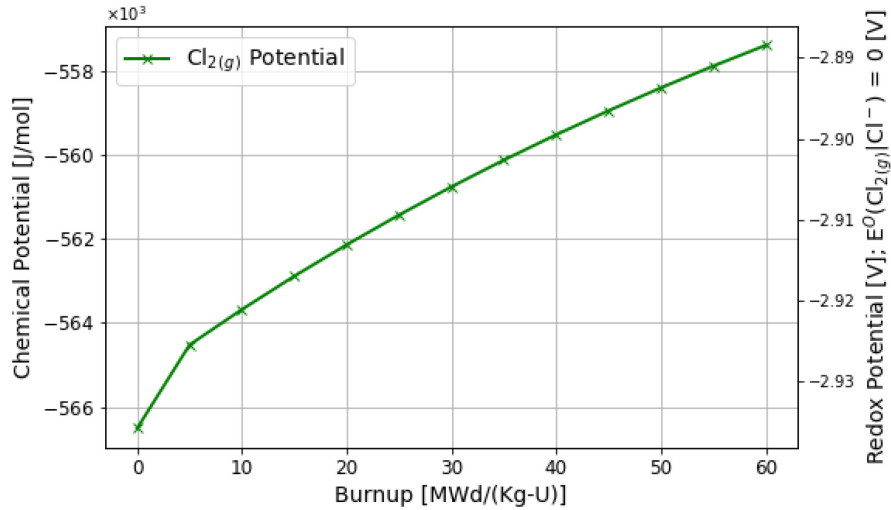


Figure 4-4. Change in chlorine potential over 60 days or 2.87 MWd/Kg-U burnup.

As with the fluoride fuel salt, the redox potential gradually increases, meaning the fuel salt is becoming more oxidizing, as anticipated. Unlike the fluoride fuel salt, however, no acceleration of redox potential occurs, meaning the redox buffer in place, likely  $\text{UCl}_4/\text{UCl}_3$ , is dictating the chlorine potential in the fuel salt. Here, uranium is a much larger fuel-salt constituent compared to the fluoride fuel salt, as seen in Table 4-1 (i.e., 33.3 mol%). Therefore, the chemical activities of the  $\text{UCl}_4/\text{UCl}_3$  buffer ratio are more stable. Additionally, this analysis, using the current thermochemical database, would suggest that the cationic charge deficiency generated from the depletion of  $\text{UCl}_3$  is less than the cationic charge deficiency that occurs from the depletion of  $\text{UF}_4$ .

Most of the key fission and activation products currently accounted for in the MSTDB-TC V2.0 for fluorides form trifluorides (e.g.,  $\text{CeF}_3$ ,  $\text{NdF}_3$ , and  $\text{PuF}_3$ ). The fission of  $\text{UF}_4$  fuel, therefore, rapidly yields a significant cationic charge deficiency. For the chloride salt, the primary fuel is  $\text{UCl}_3$ , and the key fission and activation products currently accounted for in the MSTDB-TC V2.0 for chlorides also form trichlorides (e.g.,  $\text{CeCl}_3$  and  $\text{PuCl}_3$ ). As a result, the rate of cationic charge deficiency is less pronounced for chlorides than fluorides, given the current thermochemical database. In other words, based on the currently available thermochemical data for fission and activation products included in MSTDB-TC V2.0, the missing charge from  $\text{UCl}_3$  consumption (cationic charge of 3+) is less pronounced than the missing charge from  $\text{UF}_4$  consumption (cationic charge of 4+).

Because the potential increases, not enough soluble material is available for the chlorine to dissolve. Like the oxidizing fluoride fuel-salt example, a realistic chlorine fuel-salt reactor in thermodynamic equilibrium with the structural material holding the salt will begin to dissolve the structural materials at the wall interfaces, forming corrosion products  $\text{CrCl}_2$  and  $\text{FeCl}_2$ . In this situation, Cr is available for chlorides in the MSTDB-TC V2.0. Like the fluoride fuel-salt example, where pure  $\text{Ni}_{(s)}$  was used as the structural material, here a pure  $\text{Cr}_{(s)}$  structural material with a chemical activity of 1.0 is used instead. Future work will refine this interaction by correctly accounting for the chemical activity of elements in the secondary phase model of the alloy [30].

However, because the redox potential of  $\text{CrCl}_2$  is similar to  $\text{UCl}_3$ —i.e., it is the first corrosion product to form in significant amounts, as seen in the electrochemical potential plot for chlorides in [32]—this is a reasonable approximation. Therefore, the primary and end time effect of corrosion on controlling the redox potential of the fuel salt can be modeled. That being said, the rate of corrosion occurs too quickly because the chemical activity of pure  $\text{Cr}_{(s)}$  is far greater than it would be in an alloy. The rate of chemical activity of  $\text{Cr}_{(s)}$  diffusing to the grain boundaries would also require a redox-kinetics model, instead of a thermochemical-equilibrium calculation, as used in this analysis. Here, the initial chlorine potential of the chloride fuel salt readily corrodes the pure  $\text{Cr}_{(s)}$  structural material. This effect also contributes to the diminished change in the redox potential during burnup because the chemical activity of the  $\text{Cr}_{(s)}\text{-Cr}^{2+}$  couple entering the fuel salt is significant to nearly replace the cationic charge deficiency generated through less thermochemically stable FPs.

The results for the vapor pressures in the chloride fuel salt without active redox control are shown below in Figure 4-5. As seen previously in Figure 4-3, the vapor pressures of elements are dictated by their relative concentration in the fuel salt; thus, base elements Cl, Na, and U have the highest vapor pressures in Figure 4-5. However, as the fuel salt becomes more oxidizing due to the rising redox potential, the rise in uranium volatility, despite its declining chemical activity, can be observed. In contrast to the fluoride salt, most of the elements are typically less stable in the chloride salt when comparing Figure 4-3 and Figure 4-5. This is due to the difference in the higher electronegativity of fluorine vs. chlorine. One last interesting item to note is that iodine is apparently more stable in chlorides than fluorides whereas cesium has roughly the same stability in both. This is an important understanding when considering chemical speciation during accident scenarios.

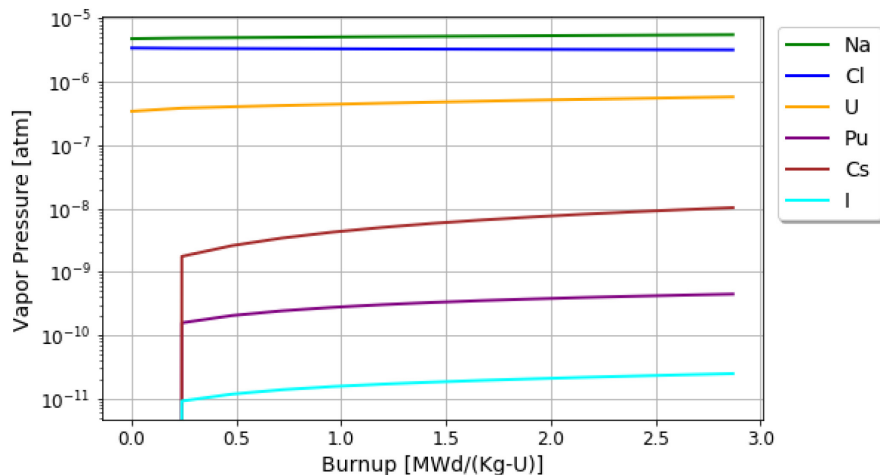


Figure 4-5. Changes in element vapor pressures in the chloride fuel salt over 60 days or 2.87 MWd/Kg-U burnup.

## 4.2. Zero-dimensional Corrosion and Active Chemistry Control Analysis<sup>f</sup>

This next subsection takes a closer look at the effect of corrosion in the zero-dimensional system and also includes a proportional-integral-derivative (PID) controller [33] to actively determine how much reducing metal should be introduced to the system to maintain a constant redox potential. The general PID-controller equation is shown as Equation (4.3).

$$u(t) = K_p e(t) + K_i \int_0^t e(\tau) d\tau + K_d \frac{de(t)}{dt}, \quad (4.3)$$

where:

$u(t)$  is the control function defined by summation of contributions from the existing error function  $e(t)$

$K_p$  is the proportional constant for the proportional error term

$K_i$  is the integration constant for the error integration term

$K_d$  is the derivative constant for the error derivative term.

Equation (4.3) can be discretized using a backward Euler finite-difference approximation in time, shown in Equation (4.4), which is implemented in the coupled-multiphysics calculation.

$$u_k = u_{k-1} + \left( K_p + K_i \Delta t + \frac{K_d}{\Delta t} \right) e_k + \left( -K_p - \frac{2K_d}{\Delta t} \right) e_{k-1} + \frac{K_d}{\Delta t} e_{k-2}, \quad (4.4)$$

where

$u_k$  is the current control value

$u_{k-1}$  is the control value of the previous time step

$\Delta t$  is the size of the time step

$e_k$ ,  $e_{k-1}$ , and  $e_{k-2}$ , correspond to the current error, and previous errors of previous time steps, respectively.

Equation (4.4) can then be used to determine the  $f_{stream,Z}^A(t)$  term of Equation (3.1) where a specific amount of reducing metal will be added to the fuel salt to control the increasing fluorine or chlorine potential of the fuel salt due to depletion. This capability is demonstrated in the following results subsection.

### 4.2.1. Fluoride Fuel-Salt Analysis

Focusing first on the fluoride fuel-salt reactor detailed in Table 4-1, the evolving redox potential of the fuel salt during the first 3.11 [MWd/Kg-U] burnup is shown in Figure 4-6. Here the solution with no redox potential control is highlighted where the chemical fluorine potential of the fuel-salt increases due to depletion. The apparent step change from 1.0 to 1.5 MWd/Kg-U of burnup is due to a loss of the  $UF_4/UF_3$  buffer in the system. A new, relatively stable redox potential is established due to the corrosion of Ni from structural materials in contact with the fuel salt [2].

---

<sup>f</sup> Portions of this subsection previously appeared as: S. A. WALKER, M. E. TANO, and A. ABOU-JAOUDE, "A Coupled Griffin and Thermochemical Method for Redox Potential Control and Off-Gas Analysis During Depletion in Molten Salt Reactors," *Proc. Intl. Conf. Math. Comp. Mthds. Nucl. Sci. Eng. (M&C 2023)*, Niagara Falls, Ontario, Canada, August 13–17, 2023, Accepted for Publication (2023) [3].

In comparison, the PID controller appears to be adjusting and finding the correct moving target for redox-potential control through the addition of Be metal (assumed to be immediately diluted into the salt in this zero-dimensional analysis) to reduce the redox potential of the fuel salt, as seen in Equation (2.6). Here a solid rod of beryllium  $Be^0_{(s)}$  is being immersed into the fuel salt, forming  $BeF_2$  and thereby altering the  $UF_4$  and  $UF_3$  redox buffer pair. This poises the chemical fluorine potential of the fuel-salt system due to the relative chemical activities in the fuel salt [2].

The effect this has on the generation or mitigation of corrosion products is visualized in Figure 4-7. Here, without active redox-potential control, the increasing fluorine potential due to depletion seen in Figure 4-6 can attack the Ni metal in structural materials in contact with the salt, creating the corrosion product  $NiF_2$  via Equation (4.1). Without redox-potential control, a nonsignificant amount of  $NiF_2$  is formed whereas, with redox-potential control by beryllium additions shown in Equation (2.6), the fluorine chemical potential is kept in check, and significant corrosion is inhibited.

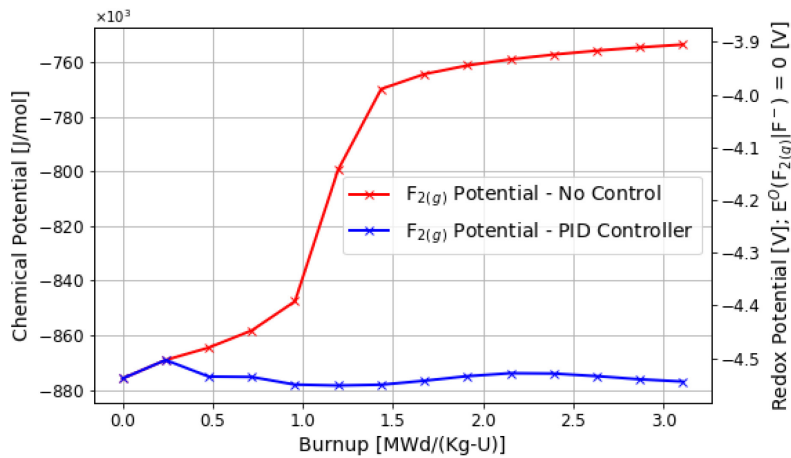


Figure 4-6. Change in fluorine/redox potential over 3.11 MWd/Kg-U burnup, with no redox control and with a PID controller.

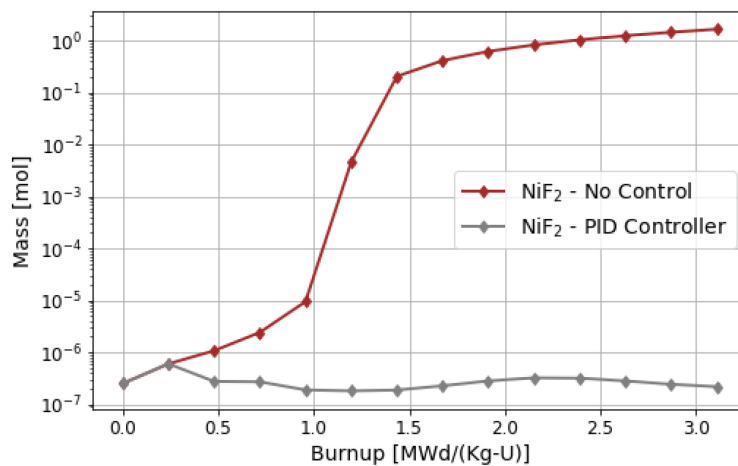


Figure 4-7. Change in corrosion-product formation over 3.11 MWd/Kg-U burnup, with no redox control and with a PID controller.



Returning to the volatilization of chemical species going to an off-gas system, the following results showcase the effect that redox control plays in determining volatility. The volatility of radionuclides with a significant radiological effect on humans (i.e.,  $\text{Cs}^{137}$  and  $\text{I}^{131}$ ) is an important item to consider for MSR system design. The results track these isotopes considering the changing redox potential of the fuel salt with and without active control.

The volatilization of key radionuclides  $\text{Cs}^{137}$  and  $\text{I}^{131}$  to the off-gas system with and without active redox control is shown in Figure 4-8. It is apparent that the changing redox potential of the fuel salt can directly impact the volatilization of species (specifically iodine due to its anionic behavior in the fuel-salt). Here, the amount of iodine arriving in the off-gas system for the uncontrolled depletion case directly follows the pattern of the increasing chemical fluorine potential shown in Figure 4-3.

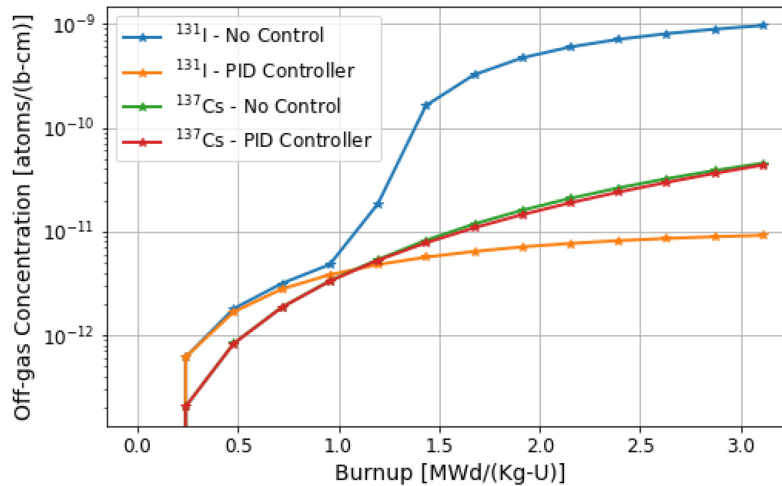


Figure 4-8. Off-gas build up in fluoride fuel salt system over 3.11 MWd/Kg-U burnup with no redox potential control and with PID controller.

Under closer inspection, the volatilization of  $^{131}\text{I}$  for the controlled case is mostly due to  $\text{CsI}_{(g)}$  vapor formation and extraction to the off-gas system. For the uncontrolled situation, the formation of  $\text{I}_{2(g)}$  vapor becomes thermodynamically more favorable, and significantly more iodine ends up in the off-gas system as a result. For the  $^{137}\text{Cs}$  case, the impact of redox potential seems negligible. This is likely because  $^{137}\text{Cs}$  vapor from  $\text{CsI}_{(g)}$  formation can be significant, but a greater source for  $^{137}\text{Cs}$  in the off-gas system is likely the extraction of noble gas  $^{137}\text{Xe}$  that comes out of the fuel salt more readily than  $\text{CsI}_{(g)}$ .

#### 4.2.2. Chloride Fuel-Salt Analysis

The chloride fuel-salt reactor, briefly detailed in Table 4-1, has changing redox potential due to depletion with and without active redox-potential control, as shown in Figure 4-9. The changing redox potential caused by depletion of the chloride system in Figure 4-9 appears to be less aggressive than in the fluoride system seen in Figure 4-6. This is likely because the  $\text{UCl}_3$  fuel is already reduced, and the generation of  $\text{UCl}_4$  is not thermodynamically favorable [2]. For the fluoride fuel salt, most of the fuel is in the  $\text{UF}_4$  state during fission; therefore, four fluorine ions need to be recaptured by soluble fission products, as opposed to only three chlorine ions that need to be recaptured [2].

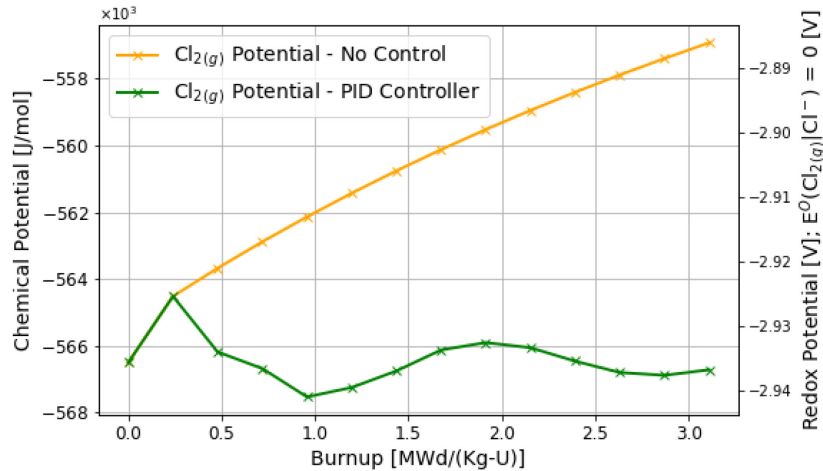


Figure 4-9. Change in chlorine/redox potential over 3.11 MWd/Kg-U burnup with no redox control and with a PID controller.

Additionally, the presence of structural materials in contact with the fuel salt provides corrosion products that are also likely to impact the solutions. Here, instead of nickel in contact with the fuel salt, chromium from the structural materials is present and ready to dissolve into the fuel salt due to the increase in chemical potential of chlorine, as seen in Figure 4-10, with an reaction analogous to Equation (4.1).

Chromium in structural materials is more thermodynamically preferable in fluoride and chloride salts than iron or nickel; therefore, the generation of measurable amounts of  $\text{CrCl}_2$ , even at initial redox potentials, is unavoidable. The formation of  $\text{CrCl}_2$  can also be greatly inhibited by active redox-potential control through the introduction of reducing metal, in this case sodium additions. Also shown in Figure 4-9 and Figure 4-10, the PID controller determines the appropriate amount of sodium to add to the system at each depletion step to successfully maintain the initial chlorine potential of the fuel salt system.

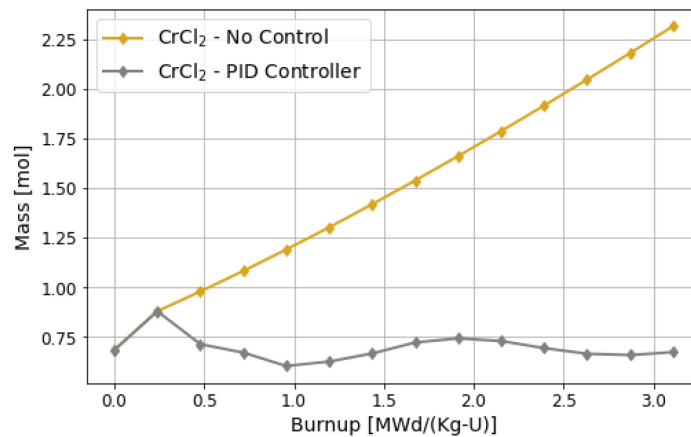


Figure 4-10. Change in corrosion product formation over 3.11 MWd/Kg-U burnup with no redox potential control and with PID controller.

Next, Figure 4-11 showcases the concentration of key radioisotopes  $^{137}\text{Cs}$  and  $^{131}\text{I}$  in the off-gas system with and without active redox-potential control in the chloride fuel salt. In contrast to the results shown in Figure 4-8, the changing redox potential of the chlorine fuel-salt system does not drastically alter the volatilization of chemical species being extracted to the off-gas system. This is because the chemical potential of chlorine, shown in Figure 4-9, does not significantly change as did the fluorine potential seen in Figure 4-6. Given a sufficiently long burnup, however, the effect of the changing redox potential is likely to become more significant, altering the volatilization of chemical species.

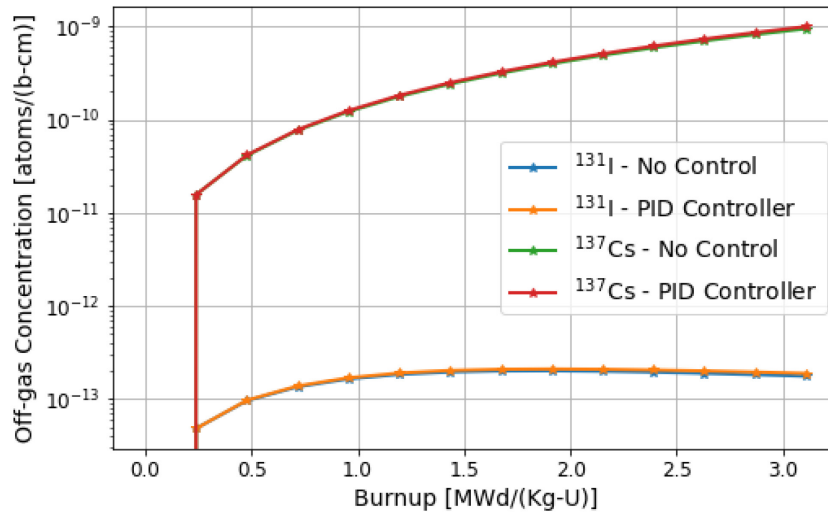


Figure 4-11. Off-gas buildup in chloride fuel salt system over 3.11 MWd/Kg-U burnup with no redox potential control and with PID controller.

Last, it is helpful to compare the behavior of these important radionuclides in both the chloride and fluoride fuel-salt systems, and this is shown in Table 4-2. Here the  $^{131}\text{I}$  is clearly more soluble in the chloride reactor system, with a negligible amount of the total  $^{131}\text{I}$  being extracted to the off-gas system with or without active redox potential control.

Table 4-2. Off-gas comparison: analysis of  $^{137}\text{Cs}$  and  $^{131}\text{I}$  in the fluoride and chloride reactors with and without PID redox-potential control.

Percentage of Radionuclides in Off-gas System		Fluoride Salt Reactor	Chloride Salt Reactor
$^{131}\text{I}$	No Control	31.10%	4.00e-4%
	PID Controller	0.29%	4.00e-4%
$^{137}\text{Cs}$	No Control	0.11%	0.17%
	PID Controller	0.11%	0.18%

Iodine-131 in the fluoride-salt system, on the other hand, greatly depends on the redox-potential control of the system, with up to 31.10% of the total  $^{131}\text{I}$  ending up in the off-gas system without redox-potential control, down to 0.29% of  $^{131}\text{I}$  extracted when the chemistry is controlled through active beryllium additions.  $^{137}\text{Cs}$  appears to be more soluble in fluoride systems than in chloride systems, but the difference is not necessarily appreciable. These results show that depletion-driven thermochemistry is critical to understand the volatilization of key radionuclides in MSR systems. Additionally, it also demonstrates the need for spatially resolved chemical species-transport analyses so that the spatial distribution of key radionuclides and their precursors (i.e.,  $^{137}\text{Xe}$ ) for mass transfer to the off-gas system can be determined.

## 5. SPATIALLY RESOLVED THERMOCHEMISTRY (PRONGHORN + THERMOCHIMICA)<sup>g</sup>

### SECTION RELATED PUBLICATIONS

The work focused on this coupling and analysis resulted in one publication listed below.

#### Conference Publications:

1. S. A. Walker, P. Bajpai, D. Schwen, M. E. Tano, and A. Abou-Jaoude, “Spatially Resolved Thermochemistry with Chemical Species Tracking in Molten Salt Reactors,” *Trans. Am. Nucl. Soc. (Winter Meeting 2023)*, Washington D.C., November 12–15, 2023, [Summary submitted for publication] (2023).

This section continues the piece-wise approach of coupling individual modeling and simulation tools to unlock new multiphysics analyses for MSRs and determine how the new capability will integrate with other NEAMS-based multiphysics codes using the MOOSE framework for MSR modeling and simulation. This new multiphysics capability shown in Figure 5-1 focuses on spatially resolved thermochemistry of MSRs with chemical-species tracking using the open-source Gibbs-energy minimizer (GEM) Thermochemica [24] and the coarse-mesh thermal-hydraulics code Pronghorn [21]. This enables spatially resolved thermochemistry, where the temperature, pressure, and fuel-salt concentration distributions in an MSR system and their effect on the thermochemical equilibrium of the system can be determined. It should be noted that a similar work was accomplished for the Virtual Environment for Reactor Applications (VERA) [19] while this work showcases this capability using NEAMS tools, based upon the MOOSE framework.

Given the coupled Pronghorn and Thermochemica capability via the MOOSE framework, this section showcases some basic results that can be visualized using the MSFR [22] as a demonstration. As stated earlier, Pronghorn calculates steady-state temperature, pressure, and elemental-composition distributions and provides these values as inputs for pointwise Thermochemica calculations of the thermochemical equilibrium of the molten-salt system. The steady-state calculation of the axisymmetric temperature and pressure fields for the MSFR is shown in Figure 5-2. Figure 5-3 showcases the steady-state velocity solution that transports species around the MSFR. Using these three thermal-hydraulic solutions, Thermochemica can resolve the spatial thermochemistry of the system.

---

<sup>g</sup> Portions of this subsection will appear as: S. A. Walker, P. Bajpai, D. Schwen, M. E. Tano, and A. Abou-Jaoude, “Spatially Resolved Thermochemistry with Chemical Species Tracking in Molten Salt Reactors,” *Trans. Am. Nucl. Soc. (Winter Meeting 2023)*, Washington D.C., November 12–15, 2023, [Summary submitted for publication] (2023).

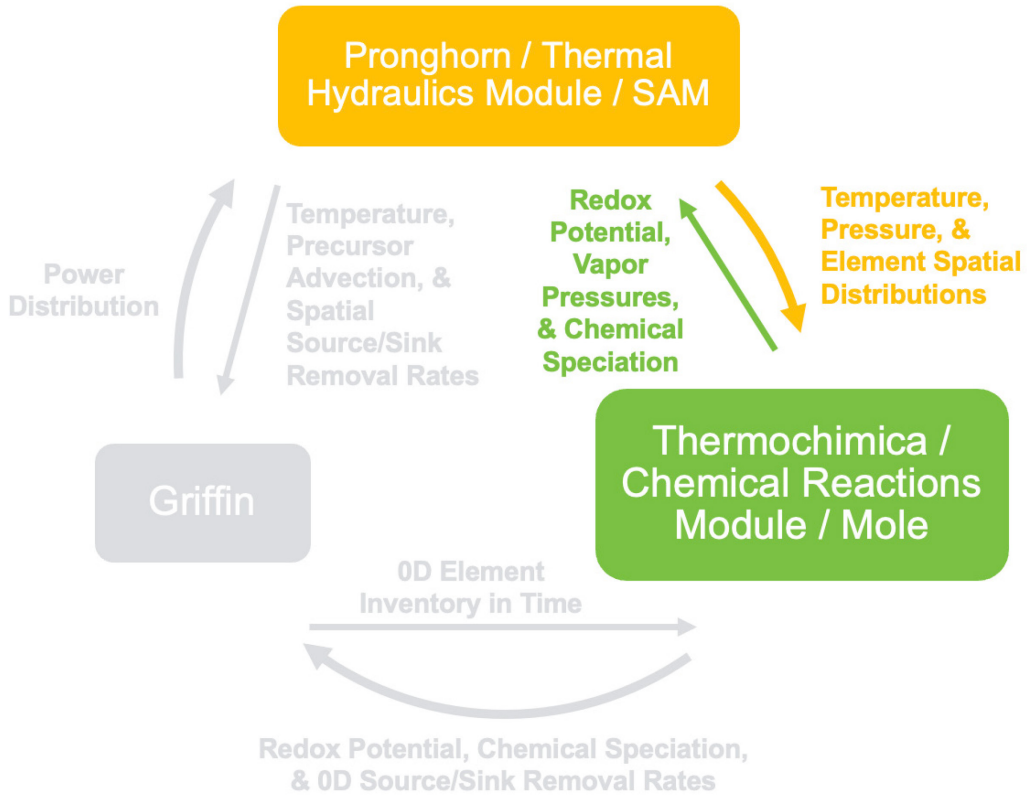


Figure 5-1. Spatially resolved thermochemistry code coupling.

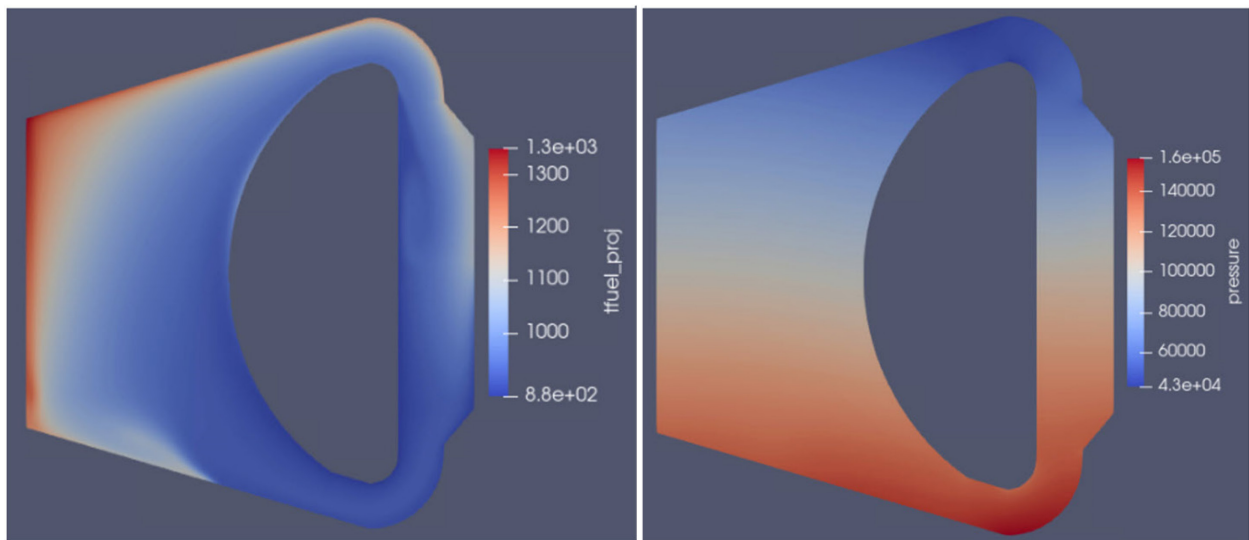


Figure 5-2. (Left) temperature field (K) and (right) pressure field (Pa).

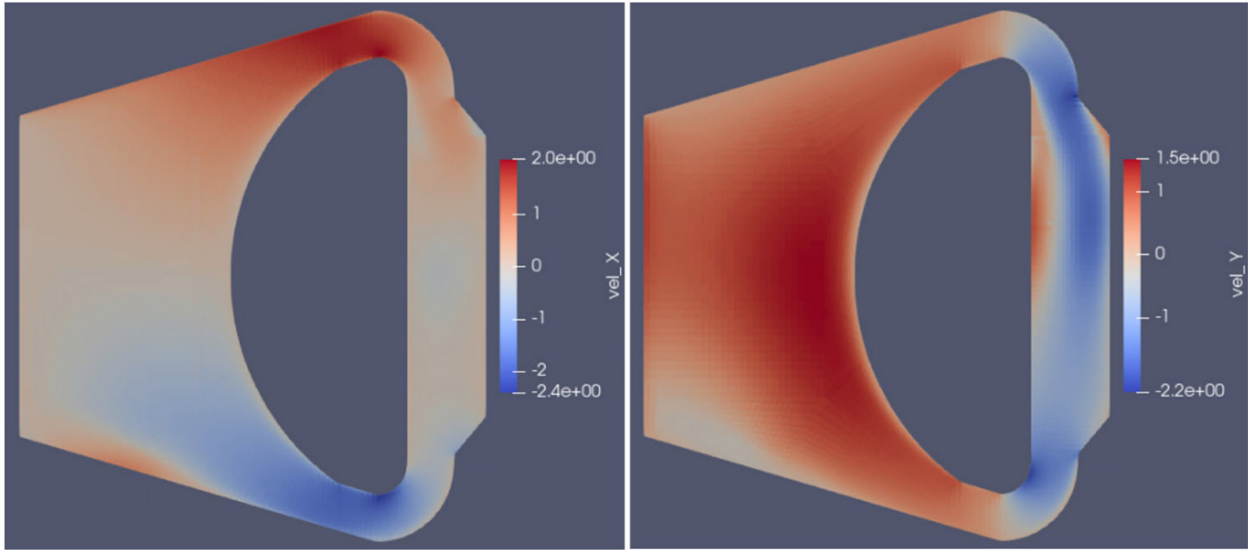


Figure 5-3. Velocity fields (m/s) in (left) x-direction and (right) y-direction.

### 5.1. Spatially Resolved Chemical Speciation and Off-Gas Analysis

The first result that can be shown using this new coupling method is spatially resolved species transport with extraction to an off-gas system. An example scenario would be gaseous-species extraction (i.e.,  $^{137}\text{Xe}$ ) in the MSFR. Figure 5-4 shows the evolving  $^{137}\text{Xe}$  spatial distribution as it undergoes extraction to an off-gas system, identified by a boundary at the top of the upper plenum of the MSFR.

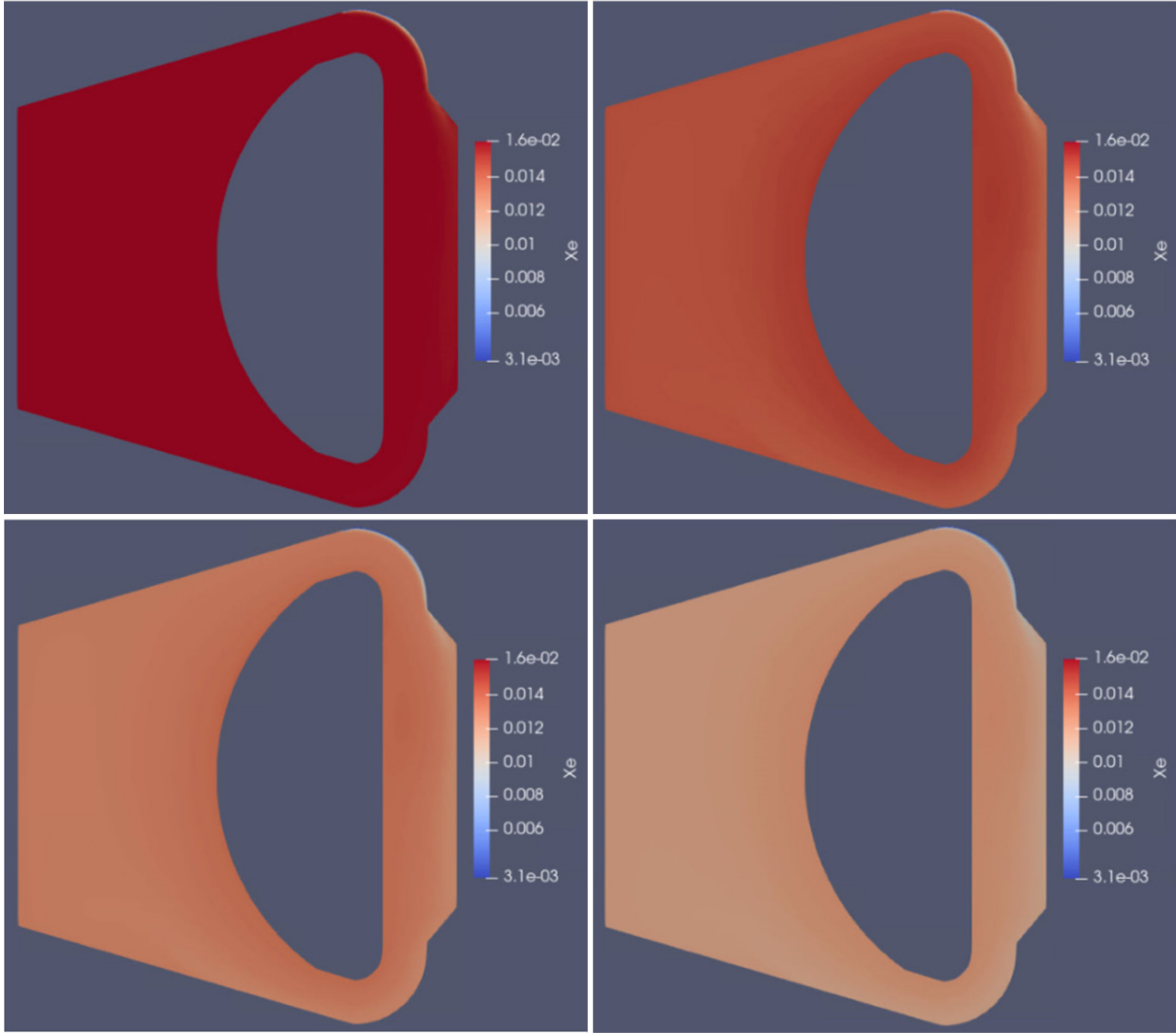


Figure 5-4. Xenon-137 distribution (mol) in the MSFR at (clockwise, from upper left) 0, 50, 100, and 150 s, respectively, showcasing decrease of gaseous species due to extraction (extraction boundary at top of upper plenum).

Here, a turbulent mass-transfer coefficient—based upon the mass-transfer equivalent of Dittus-Boelter heat-transfer coefficient [34]—was implemented to model species transport to the off-gas system boundary, shown in Equation (5.1):

$$K = 0.023 \frac{D}{d} \left( \frac{\rho d v}{\mu} \right)^{0.8} \left( \frac{\mu}{\rho D} \right)^{0.4} \quad 0.6 \leq Sc \leq 160; \quad Re_d > 10,000 \quad (5.1)$$

where:

$D$  is the diffusion coefficient of the species in the fluid

$d$  is the hydraulic diameter of the pipe

$v$  is the velocity

$\mu$  is the viscosity

$\rho$  is the density of the fluid respectively.

The mass transfer coefficient  $K$  [m/s] is then used in a mass flux boundary condition shown in Equation (5.2):

$$m'' = K \cdot (c_{i,interface} - c_{i,bulk}) \quad (5.2)$$

where

$m''$  is the mass flux (i.e., [moles/(s-m<sup>2</sup>)])

$c_{i,interface}$  is the molar concentration of species at the interface

$c_{i,bulk}$  is the molar concentration of the same species in the bulk region of the flow.

Then Equation (5.2) is applied as a boundary condition in the species-transport, Equation (3.6), for a specific off-gas system boundary for volatile species like <sup>137</sup>Xe. Because <sup>137</sup>Xe is the precursor of <sup>137</sup>Cs, the extraction of <sup>137</sup>Xe has a direct influence on the distribution of <sup>137</sup>Cs, as seen in Figure 5-5.

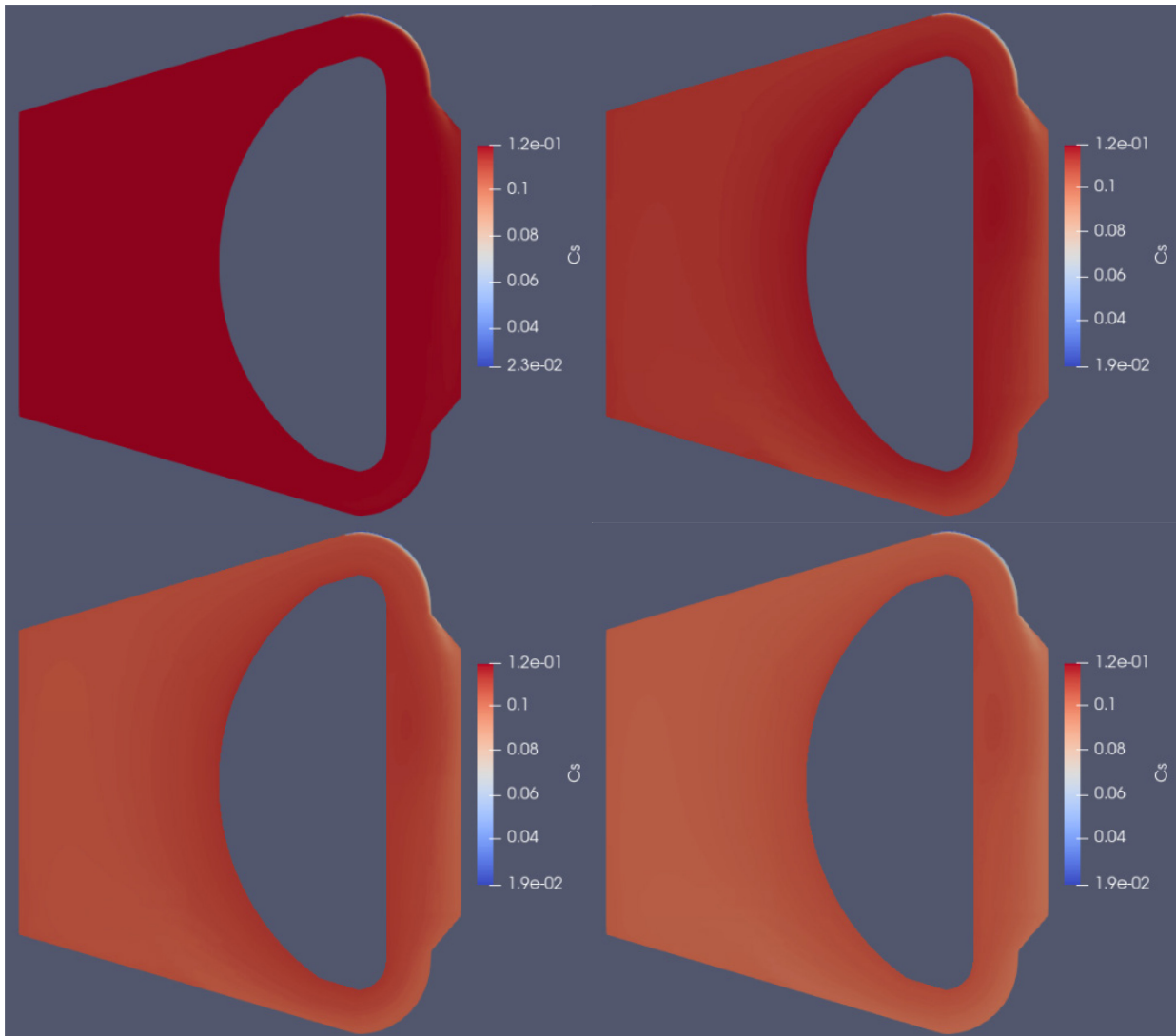


Figure 5-5. Cesium-137 (mol) distribution in MSFR at (clockwise, from upper left) 0, 50, 100, and 150 s, respectively, showcasing decrease of daughter species due to parent extraction (extraction boundary at top of upper plenum).



Lastly, vapor pressures calculated by Thermochemica in this region can be examined to determine what other species may enter the gas phase and be extracted along with noble gases. The example of  $\text{CsI(g)}$  and  $\text{I}_2(\text{g})$  are shown in Figure 5-6. Here the decrease in Cs due to Xe extraction can be clearly seen at the boundary of the off-gas system when analyzing the  $\text{CsI(g)}$  vapor pressure. Due to this decrease in Cs, the relative amount of  $\text{I}_2(\text{g})$  vapor pressure increases in this region at the boundary. It should be noted however that the  $\text{I}_2(\text{g})$  vapor pressure is still orders of magnitude smaller than the  $\text{CsI(g)}$  vapor pressure due to the reduced fuel-salt redox potential. These results correspond to a beginning of life fuel salt redox potential shown in Figure 4-3 where the  $\text{I}_2(\text{g})$  vapor pressure is still minimized by the fuel salt equilibrium chemistry and before it increases due to depletion.

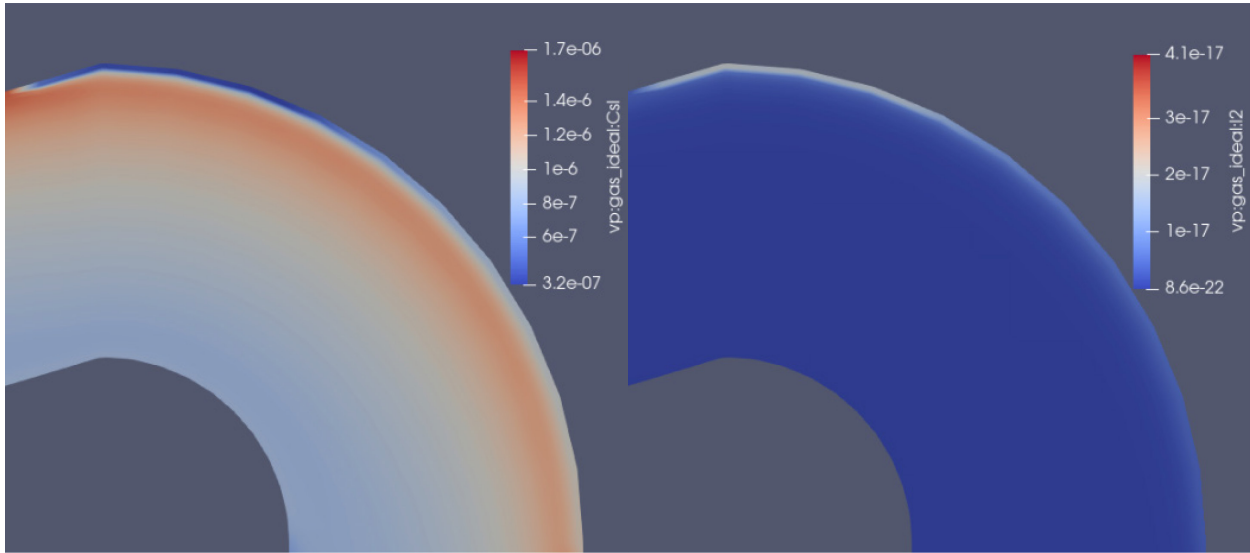


Figure 5-6. Vapor pressure (atm) of (left)  $\text{CsI}$  and (right)  $\text{I}_2$  in the MSFR, showcasing relative decrease of Cs and relative increase of I vapor pressure at boundary.

## 5.2. Spatially Resolved Corrosion and Active-Chemistry Control

The next result that can be shown with this new coupling method is spatially resolved corrosion with and without active-chemistry control. An example scenario would be the corrosion of structural materials in thermochemical equilibrium with a fuel salt that generates corrosion species (e.g.,  $\text{NiF}_2$ ) in the MSFR, according to Equation (4.1). This process can be partially mitigated by controlling the redox potential of the fuel salt via reducing-metal additions, seen in Equation (2.6).

Like the gaseous species extracted in the previous subsection using Equation (5.1) and Equation (5.2), this analysis calculates  $\text{BeF}_2$  at an interface where extra beryllium is being introduced to actively control the chemistry of the fuel-salt system. It then tracks this new  $\text{BeF}_2$  concentration as it mixes in the MSFR. The introduction of beryllium into the MSFR can be seen in Figure 5-7. Here the inlet boundary is set at the bottom of the MSFR lower plenum.

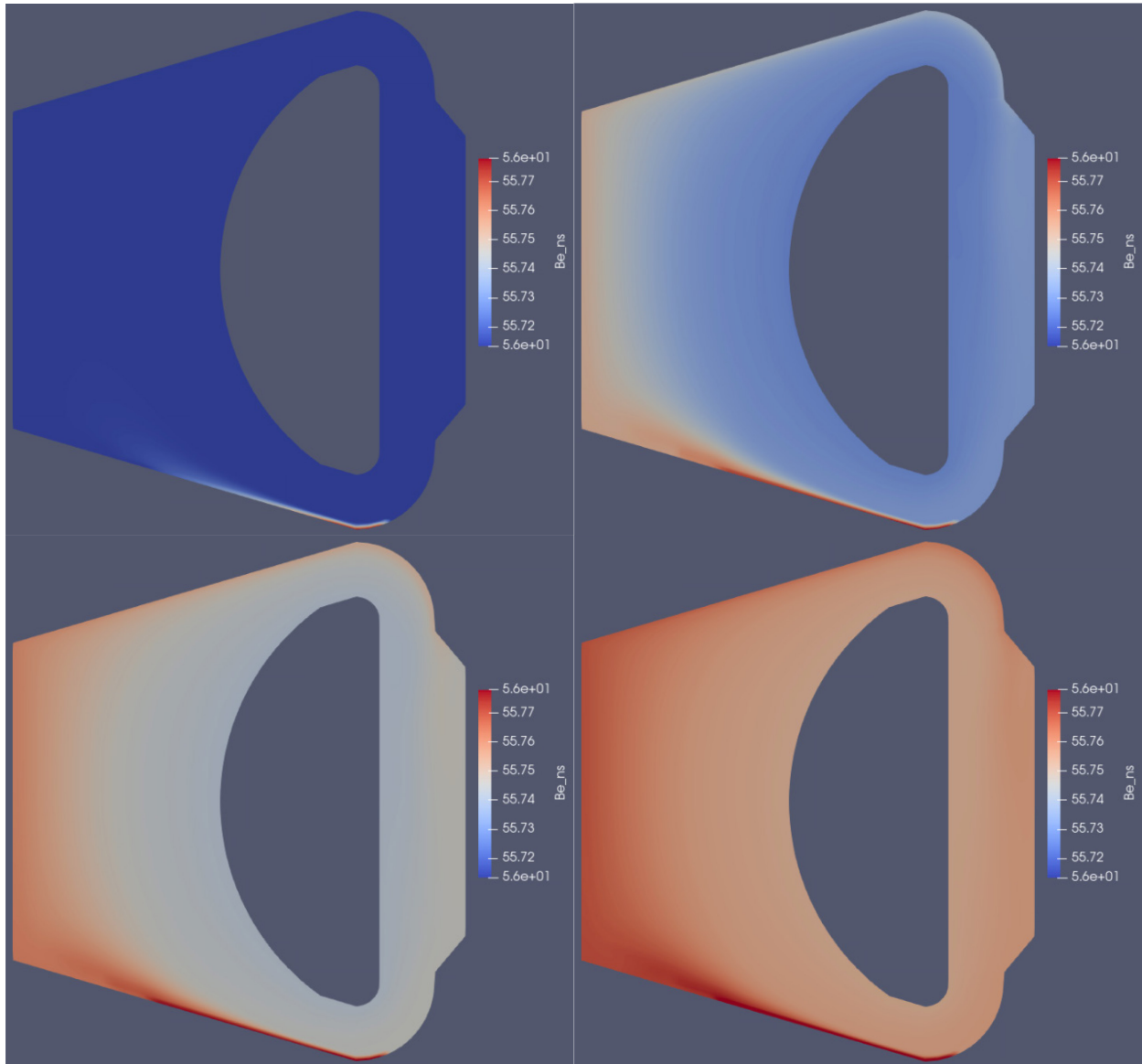


Figure 5-7. Be distribution (mol) at (clockwise, from upper left) 0, 50, 100, and 150 s, respectively, showcasing beryllium addition to MSFR system (inlet at bottom of lower plenum).

As seen in Figure 5-7, the beryllium inlet at the boundary is advected into the MSFR system, mixing and diffusing towards a new thermochemical and thermal-hydraulic steady state. The reductive effect of introducing beryllium on the redox potential of the fuel-salt can be seen in Figure 5-8, which captures the changing fluorine potential due to the beryllium addition. Here the fluoride ( $F^-$ ) potential steadily decreases from  $\sim -460,000$  to  $\sim -465,000$  J/mol, corresponding to a final fluorine ( $F_2$ ) potential of  $\sim -930,000$  J/mol as the additional  $BeF_2$  circulates throughout the MSFR system.

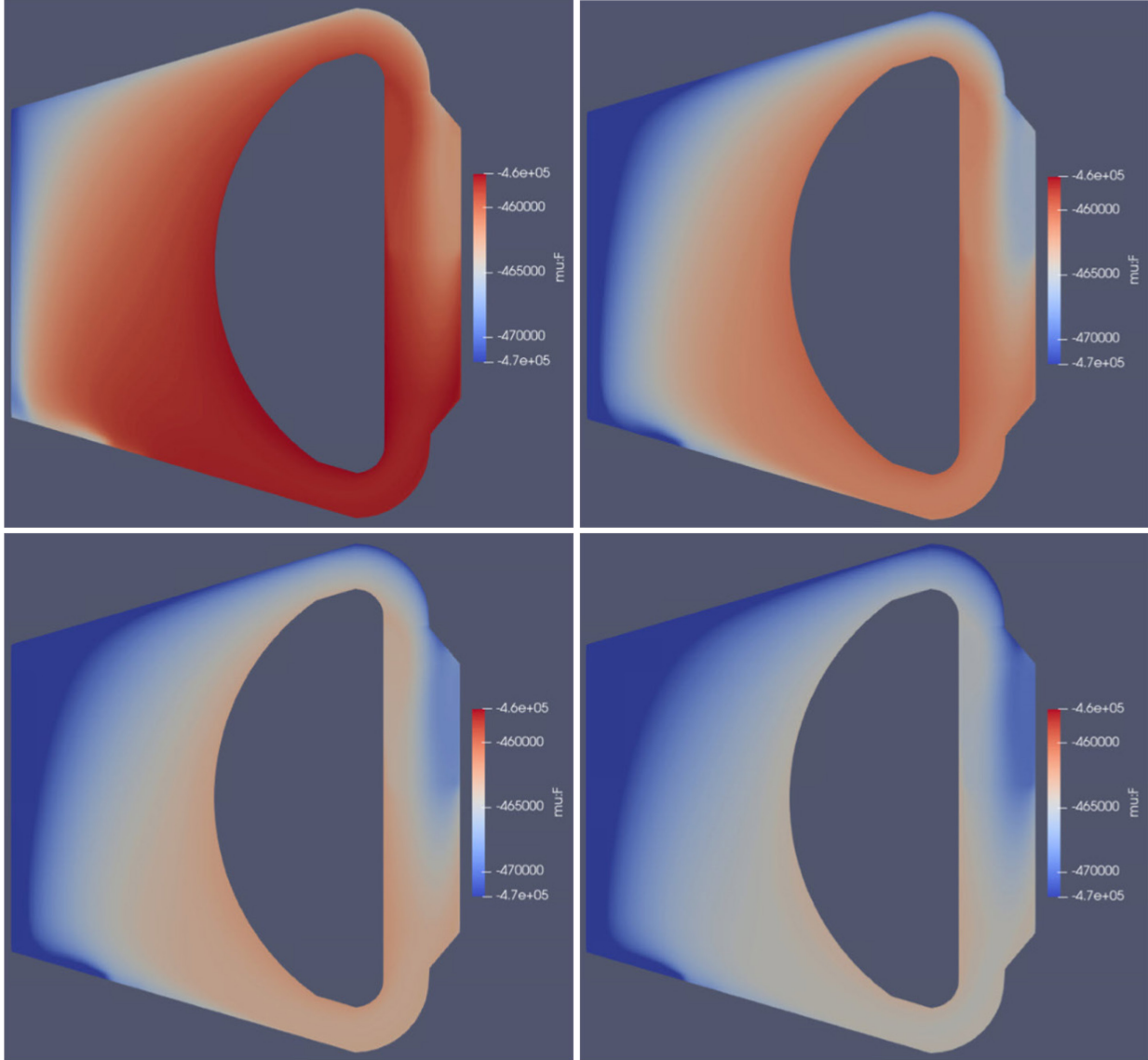


Figure 5-8. Corresponding fluoride (F<sup>-</sup>) potential (J/mol) at (clockwise, from upper left) 0, 50, 100, and 150 s, respectively, showcasing beryllium reduction of MSFR fuel salt – inlet at bottom of lower plenum.

Last, the effect of introducing beryllium into the MSFR on the distribution of the corrosion product NiF<sub>2</sub> can be seen in Figure 5-9. Here, due to the introduction of beryllium's altering the redox potential, beryllium reduces NiF<sub>2</sub> to Ni<sub>(s)</sub> via Equation (5.3):



This process never completely reduces the NiF<sub>2</sub> because remaining NiF<sub>2</sub> corrosion product is driven more by high-temperature corrosion in the core than by an oxidizing redox potential in the fuel salt. The effect of depletion on the redox potential of the fuel salt and NiF<sub>2</sub> corrosion, in addition to high-temperature corrosion, requires the incorporation of depletion, which is covered in the next section.

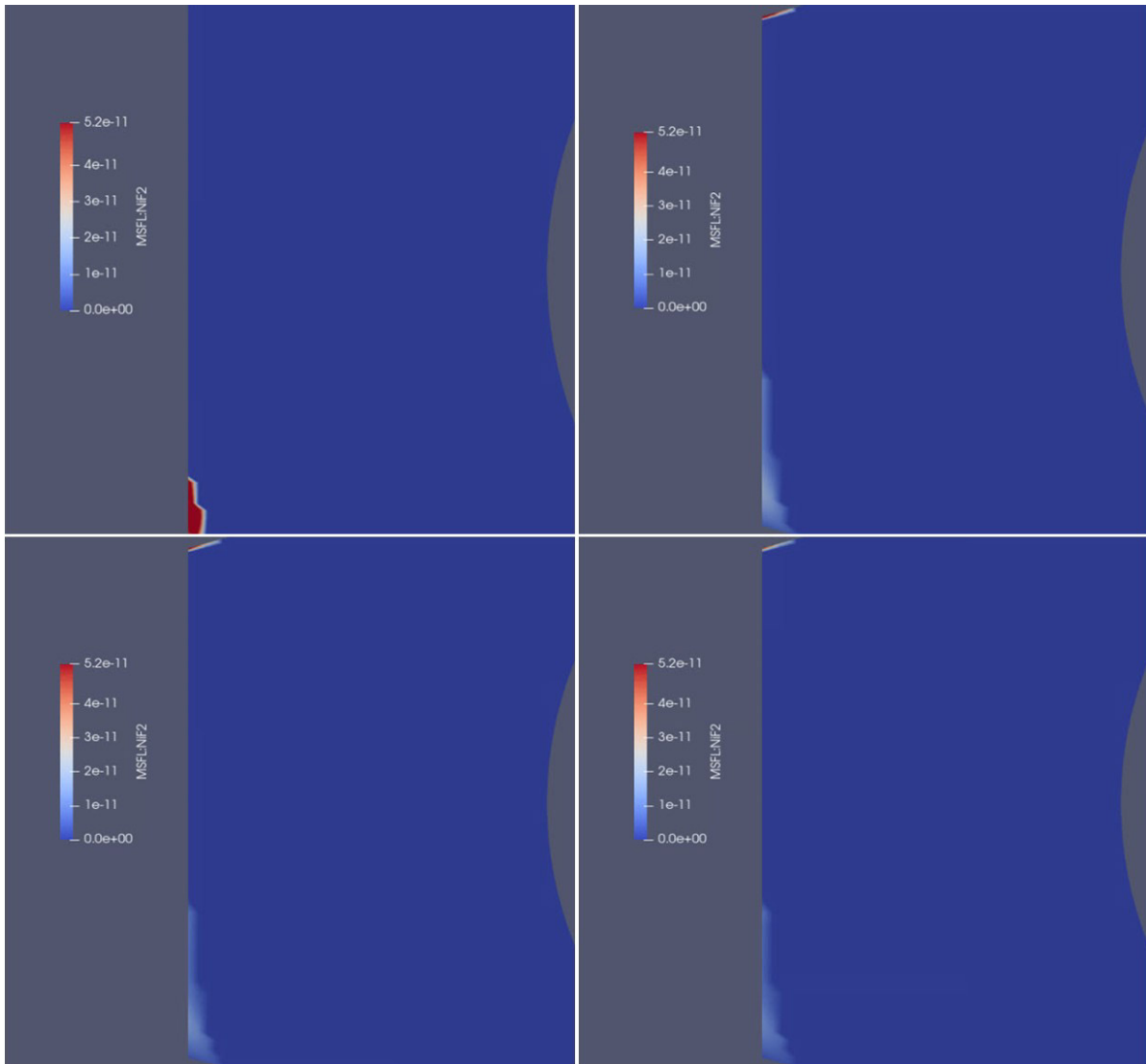


Figure 5-9. Corresponding  $\text{NiF}_2$  distributions (mol) at (clockwise, from upper left) 0, 50, 100, and 150 s, respectively, showcasing loss of  $\text{NiF}_2$  to  $\text{Ni}_{(s)}$  precipitant due to beryllium addition reducing MSFR fuel salt.

## 6. NEAMS FRAMEWORK: DEPLETION-DRIVEN SPATIALLY RESOLVED THERMOCHEMISTRY (GRIFFIN + PRONGHORN + THERMOCHEMICA)

**SECTION RELATED PUBLICATIONS**

The work focused on this coupling and analysis will result in one publication listed below.

**Journal Publications:**

1. S. A. WALKER, M. E. TANO, A. ABOU-JAOUDE, and P. BAJPAI, "Multiphysics Chemical Species Transport Framework for Molten Salt Reactor Analysis," *Eur. Phys. J. Nucl. Sci. Tech.*, Topical Issue on modeling breakthroughs for Advanced Nuclear Reactors, [Manuscript in Preparation] (2024).

This final step to complete the state-of-the-art framework involves coupling all three physics—i.e., depletion, thermal hydraulics, and thermochemistry—to enable depletion-driven, spatially resolved thermochemistry of MSRs for chemical species-transport analyses shown in Figure 6-1. This final results section looks at the effect of depletion on altering spatially resolved redox potential of the fuel salt and its impact on corrosion-product formation and changes in chemical vapor-pressure speciation.

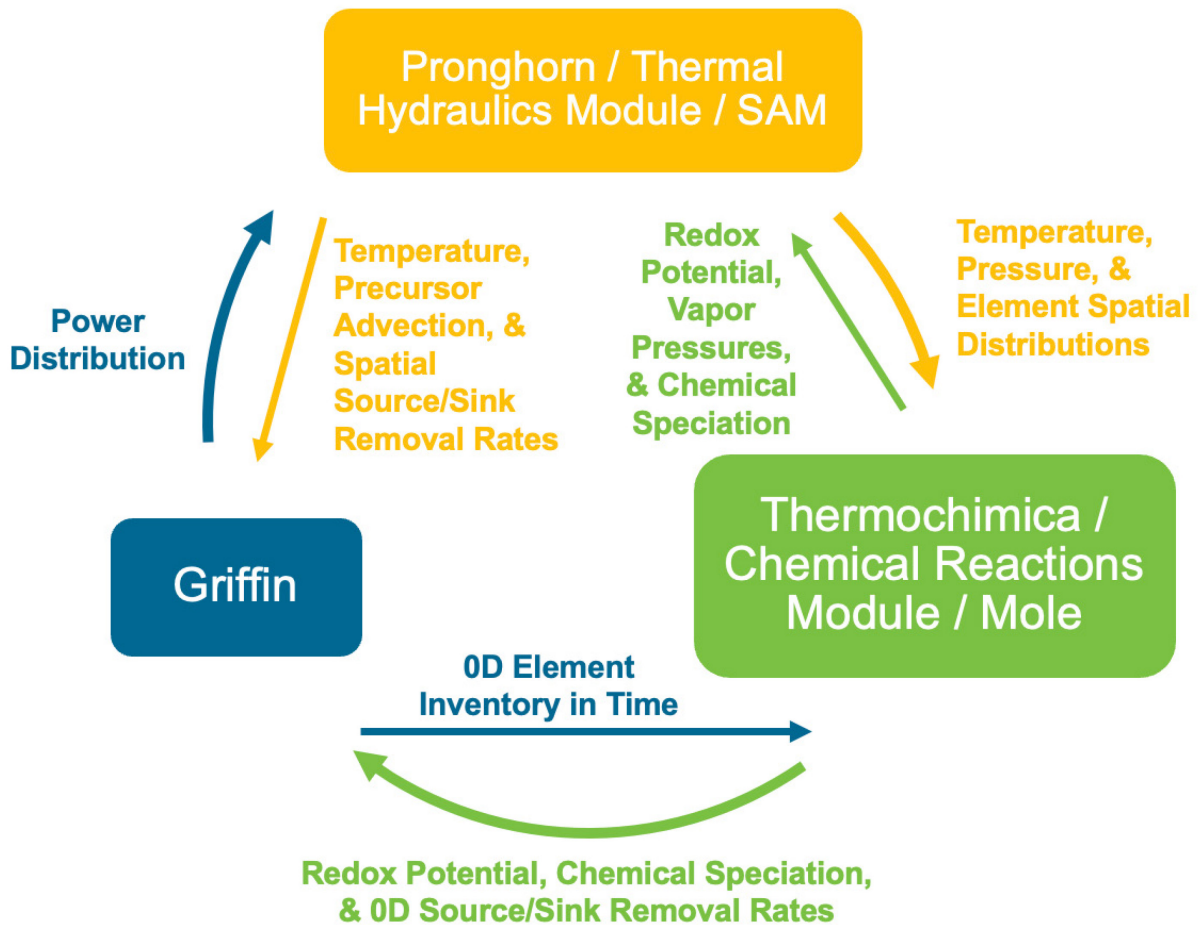


Figure 6-1. Depletion-driven spatially resolved thermochemistry code coupling.

Looking first at how depletion changes the spatially resolved redox potential of the fuel salt, Figure 6-2 shows the changing fluorine potential during burnup. Here the fluorine ( $F_2$ ) potential of the salt is rapidly increasing roughly from  $-920,000$  to  $-720,000$  J/mol due to the changing chemical composition driven by depletion.

This oxidizing process appears to slow in the bottom panels of Figure 6-2. The reason for this can be seen clearly in Figure 6-3 which depicts the formation of  $NiF_2$  due to corrosion of structural materials in thermochemical equilibrium with the fuel salt. This is an analogous result to a spatially resolved version of Table 4-1 and Figure 4-6. Similar to these zero-dimension analyses, the corrosion of  $Ni_{(s)}$  to  $NiF_2$  controls the redox potential—albeit now the spatial effects of temperature and corrosion product distribution can be fully visualized in Figure 6-2 and Figure 6-3. Nevertheless, it is important to note that the incorporation of spatially resolved temperature distributions in the MSFR greatly affects the rate at which redox conditions change during depletion.

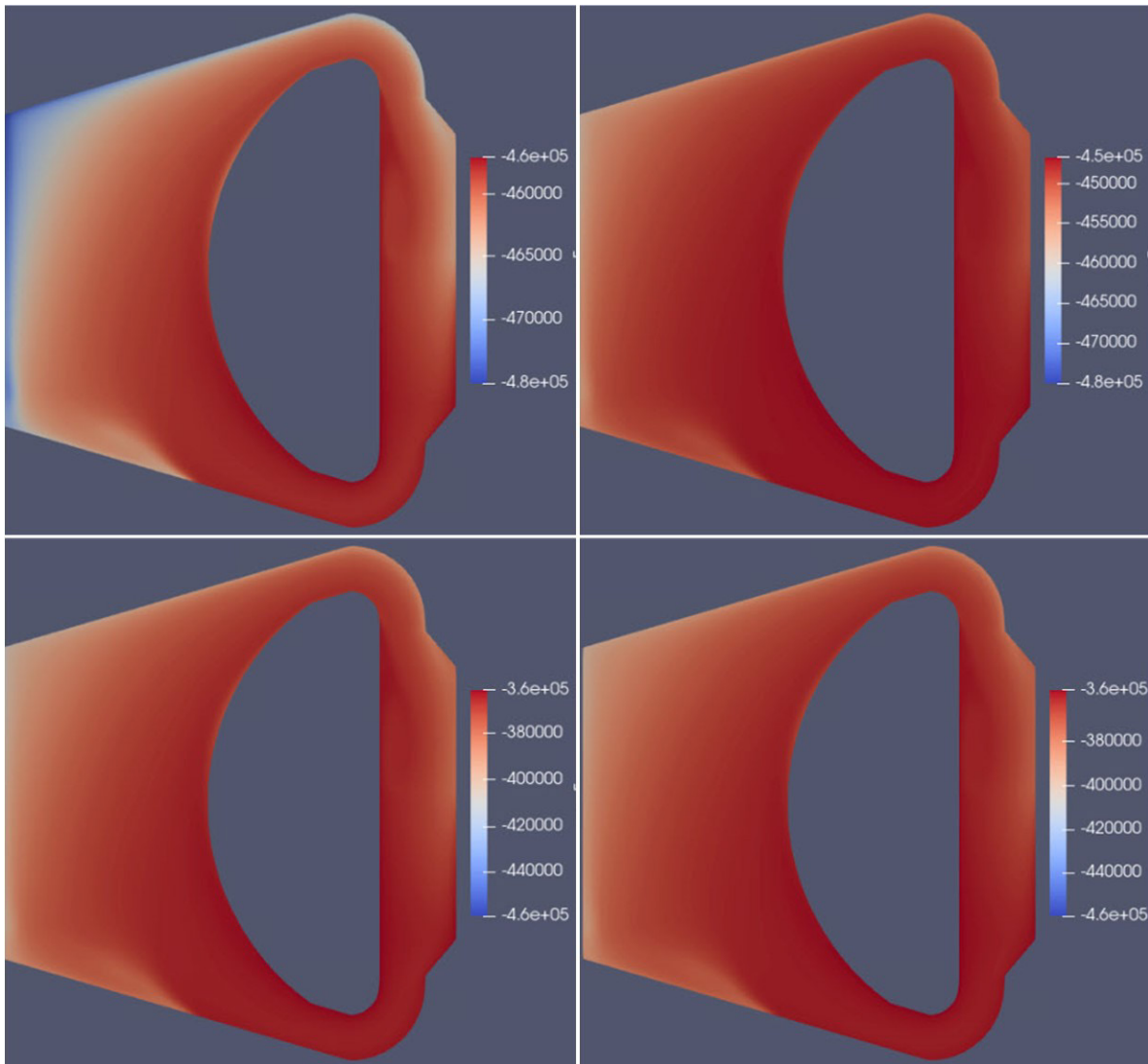


Figure 6-2. Fluoride ( $F^-$ ) potential (J/mol) at (clockwise, from upper left) 0.024, 0.048, 0.096, and 0.239 MWd/Kg-U, showcasing the oxidizing effect of depletion on MSFR fuel salt.



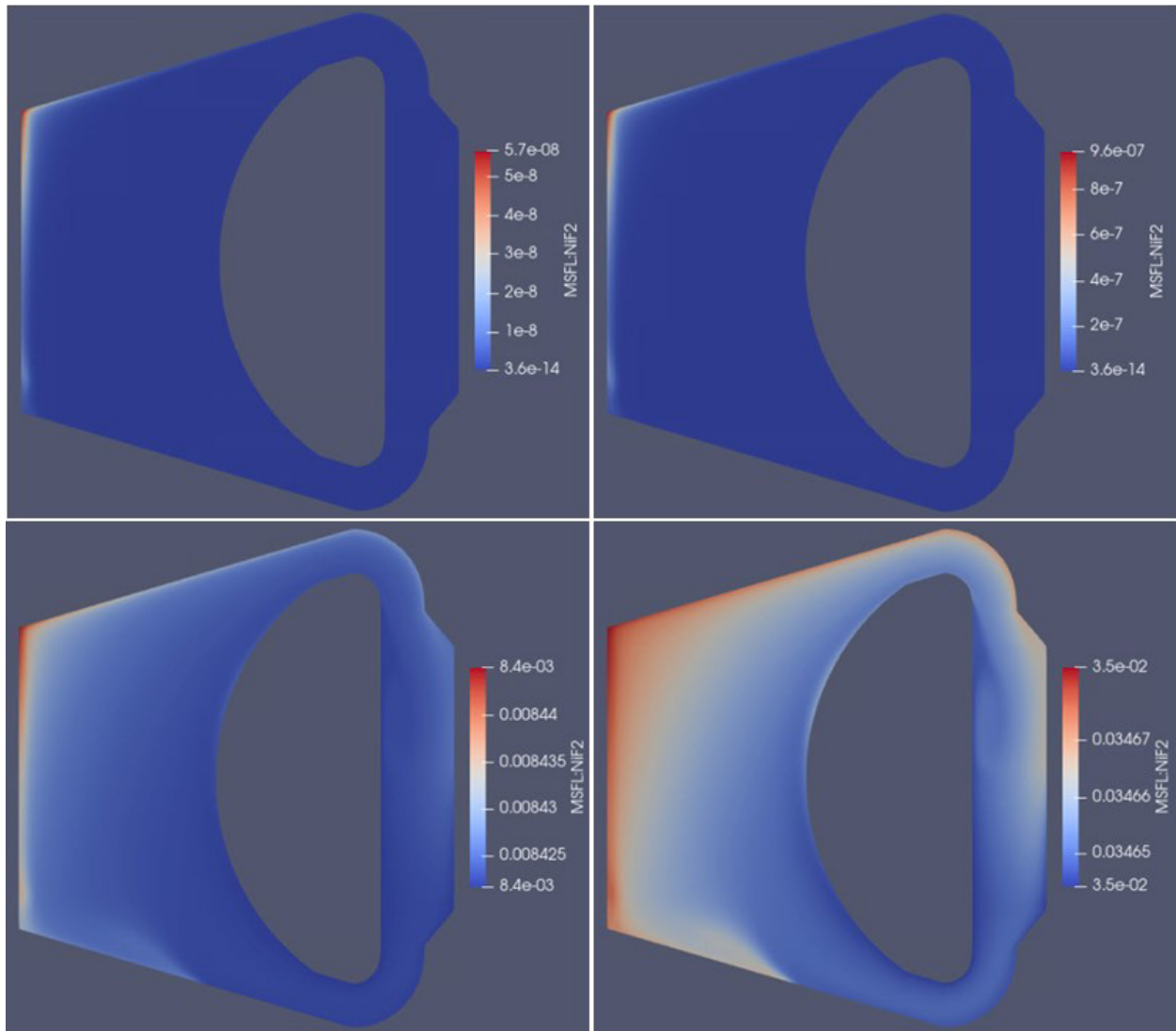


Figure 6-3.  $\text{NiF}_2$  distributions (mol) at (clockwise, from upper left) 0.024, 0.048, 0.096, and 0.239 MWd/Kg-U, showcasing gain of  $\text{NiF}_2$  due to depletion oxidation.

Turning towards chemical species volatilization, Figure 6-4 showcases the oxidizing effect that depletion has on increasing the vapor pressures of  $\text{CsI(g)}$  in the MSFR. Here the vapor pressure of  $\text{CsI(g)}$  increases from  $\sim 9.9 \times 10^{-7}$  to  $\sim 7.9 \times 10^{-5}$  [atm] due to depletion. This is a spatially resolved analogous result to Figure 4-3 which showcases that vapor pressure of I greatly increases due to the oxidizing change in redox potential.

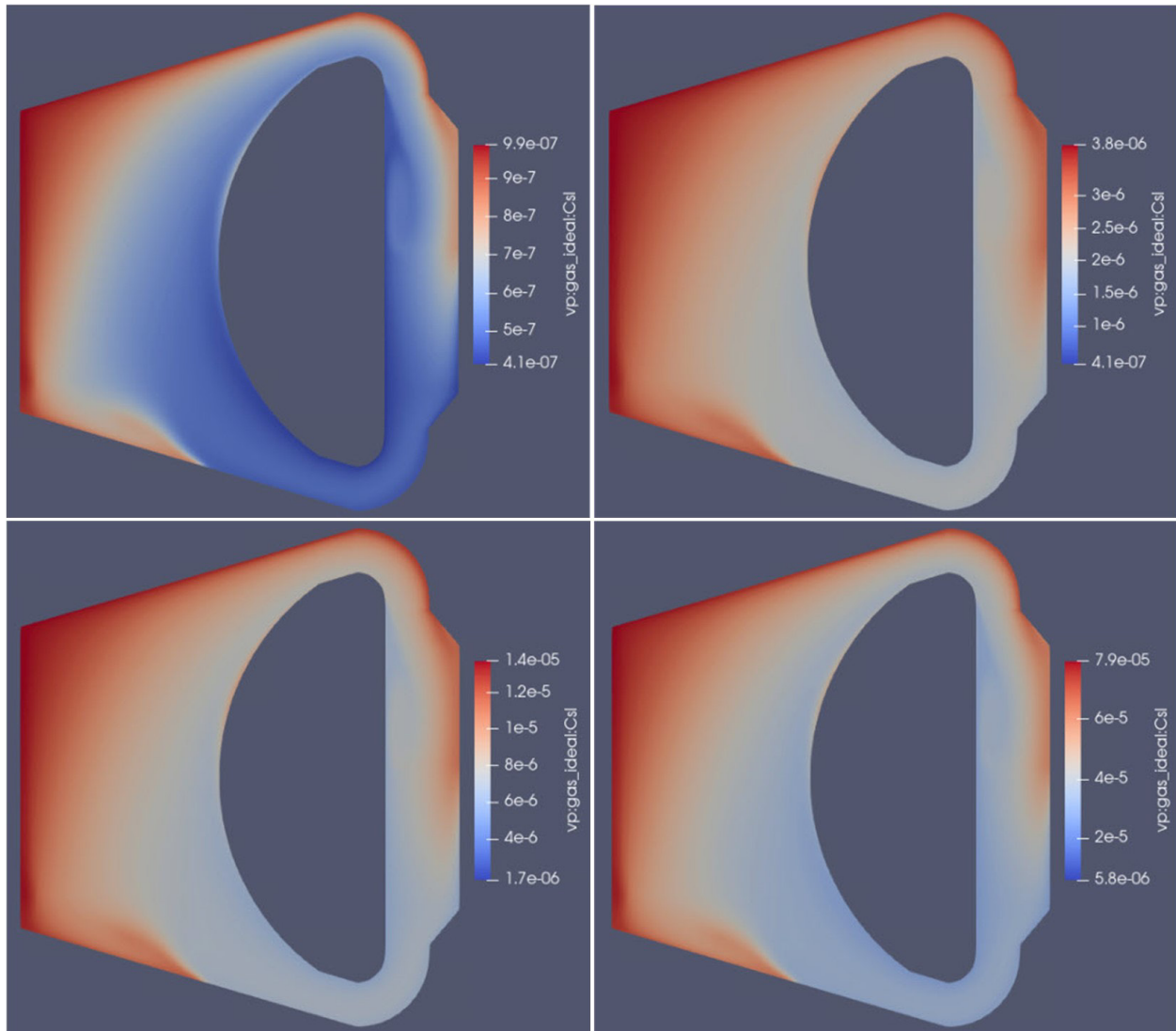


Figure 6-4. Vapor pressure (atm) of CsI distributions at (clockwise, from upper left) 0.024, 0.048, 0.096, and 0.239 MWd/Kg-U, showcasing volatilizing effect of depletion.

This effect is even more pronounced in the increasing spatial resolution of the vapor pressure of  $I_{2(g)}$  shown in Figure 6-5. Here the vapor pressure of  $I_{2(g)}$  increases, approximately from  $3.3e-11$  to  $1.3e-02$  atm, due to depletion-driven changes in the redox potential of the fuel salt.

A few items to note from this analysis are that  $I_{2(g)}$  forms more readily in regions with the highest redox potential. This can be visualized by comparing Figure 6-5 to Figure 6-2. Additionally, it is important to understand that vapor-pressure distribution calculations like these are only useful when stable liquid/gas interfaces are present. This would imply that a liquid/gas boundary to an off-gas system should be used at a specific location, as shown in Section 5, or some homogenized surface area from noble-gas bubbles present in the MSFR bulk or at a liquid/solid/gas interface should be incorporated for mass-transfer calculations.



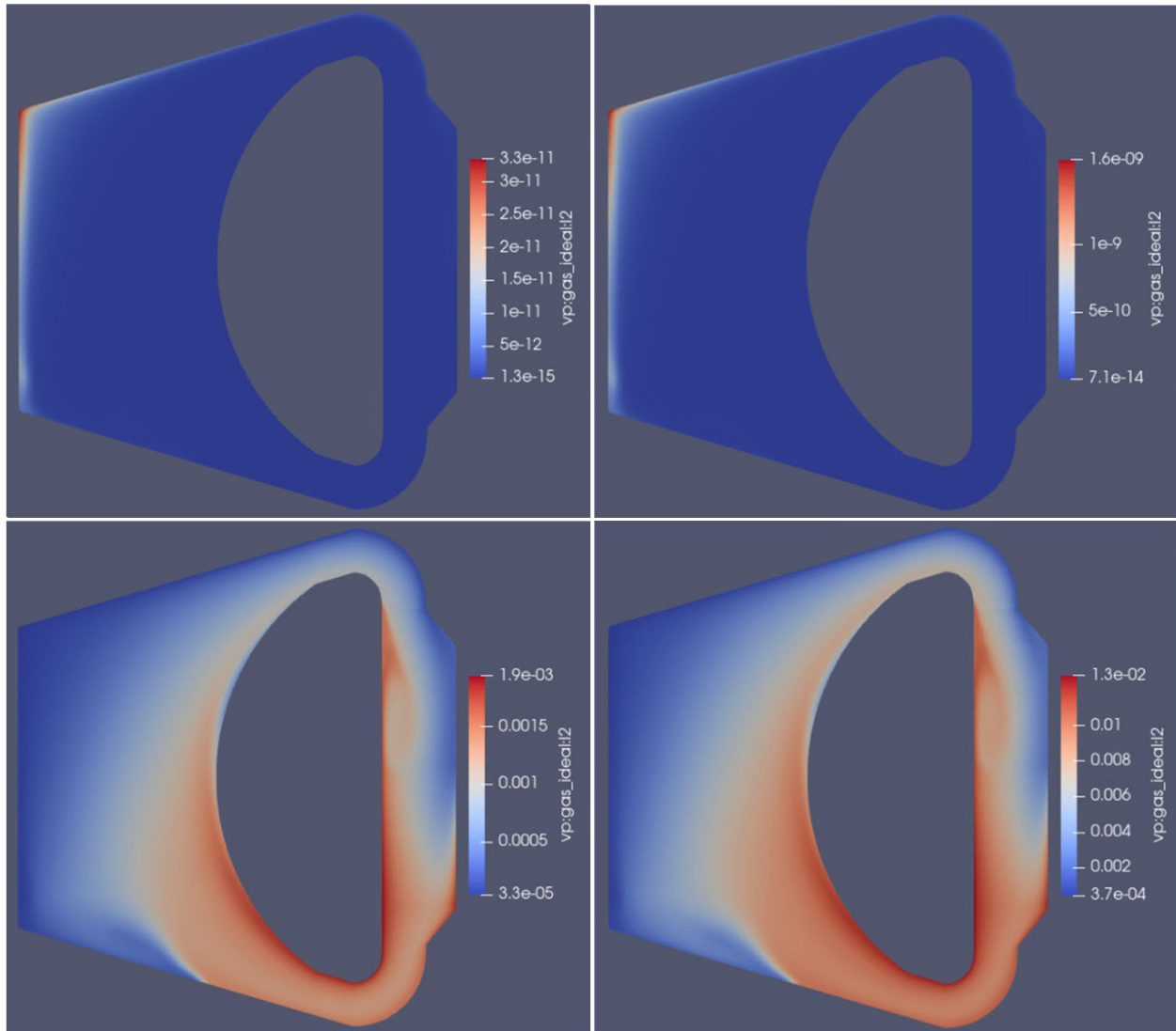


Figure 6-5. I<sub>2</sub> vapor pressure [atm] distributions at (clockwise, from upper left) 0.024, 0.048, 0.096, and 0.239 MWd/Kg-U, showcasing volatilizing effect of depletion.

Last, through the depletion-driven, spatially resolved thermochemistry species-tracking capability, the amounts of nuclides extracted to an off-gas system during depletion can be further characterized for various off-gas extraction systems. Using the mass-transfer model described in Equations (5.1) and (5.2), the effect of extracting <sup>137</sup>Xe gas on daughter product <sup>137</sup>Cs can now be visualized for a simple liquid-gas interface off-gas system, as shown in Table 6-1. When comparing Table 6-1 with Table 4-2, it is apparent that the spatial tracking and mass transfer of <sup>137</sup>Xe is a dominant effect in determining the amount of <sup>137</sup>Cs that will accumulate in the off-gas system. Ongoing work will further resolve these transport processes for other radiologically significant nuclides in forthcoming publications.

Table 6-1. <sup>137</sup>Cs off-gas analysis after 3.11 MWd/Kg-U burnup of fluoride fuel salt.

Radionuclide in Off-gas System	Concentration in OG System [atoms/b-cm]	Percentage in OG System
<sup>137</sup> Cs	2.36e-09	3.56%

## **7. FUTURE WORK AND SYNERGISTIC COLLABORATIONS**

The work accomplished this FY paves the way to a whole suite of new analyses in future work and collaborations. This section briefly explores the most-imminent tasks that should be performed in the next FY and introduces many more that naturally follow, building upon this work, given time and resources.

### **7.1. Validation of Framework via MSRE Data using MSTDB V3.0**

The most pressing task of FY-24 involves using the most up-to-date data available from MSTDB-TC V3.0. The numerous database improvements of MSTDB-TC V3.0 will enable work on validating the existing framework against data from the MSRE.

Previously, modeling the MSRE fuel salt was not possible because Zr was missing from the MSTDB. Zr was a significant fuel-salt component (and fission product) making up ~5% of the MSRE fuel salt; thus, not having this element in the database precluded any sort of direct comparison against the existing MSRE data. Zr is also expected to exist in the fuel salt, with an ion charge of 4+, meaning it is critical in determining the fluorine potential of the fuel salt.

It is expected that that  $ZrF_4$  will be included in the upcoming release of MSTDB-TC V3.0. This will enable the validation work of the existing framework to begin in FY-24 using the MSRE data observed in Table 2-1 [12] and other MSRE data as a first-of-its-kind MSR-chemistry modeling benchmark [35].

### **7.2. Informing and Coupling with System-Code Analysis**

A second task for FY-24 involves informing system-code analysis for chemical-species generation, behavior, and transport. Some possible examples and ongoing collaborations for this work would be to collaborate with Sandia National Laboratory to develop higher-to-lower fidelity informed closure models via NEAMS-compatible MELCOR [36] modeling for system-level and accident-scenario analyses.

Additional avenues that may be worth investigating include new collaborations with Argonne National Laboratory (ANL) to couple with System Analysis Module (SAM) species transport or with ORNL's Mole species transport via a domain overlap approach [36]. This would allow for multidimensional species transport, coupled with spatially resolved thermochemistry, seen in Sections 5 and 6 to accurately inform system-level species-transport codes.

### **7.3. Framework Enhancements and New Applications**

A third task for FY-24 would be to perform some natural-progression upgrades on the existing framework as new capabilities are developed via the NEAMS program. Some of these upgrades already under active development could be incorporated into the state-of-the-art framework in FY-24. These include 1) material deposition and dissolution on interfaces via MOOSE, 2) incorporating the Poison-Nernst-Planck (PNP) and Butler-Volmer (BV) models for redox reaction kinetics [38], 3) two-phase-flow species tracking in Pronghorn, and 4) spatially resolved decay heat and activity modeling of nuclides.

Additionally, new analysis applications of the framework listed on Table 1-1 should be pursued. Possible applications include a more-thorough analysis of MSR dynamics, incorporating  $^{135}\text{Xe}$  transport during normal and accident-transient scenarios. Additionally, future collaborations with the ANL in use of the framework for source-term analyses is already underway. Last, a natural progression to use the multiphysics and multiscale framework for safeguards and chemical forensic analysis is anticipated.

### **7.4. Future Work for Later Years**

As the framework is further validated, direct collaboration with experimentalists is envisioned. Already experimentalists at INL hope to gain insight from using this framework to design pyroprocessing units.

Future work will build upon these collaborations with experimentalists to employ the framework in determining uncertainty and sensitivity of missing data to guide data collection and database formation and define measurement requirements for instrumentation and control systems for experimental reactors and reactor components. Eventually, the development of digital twins for laboratory experiments and experimental reactor deployments can be envisaged.

## 8. SUMMARY AND CONCLUSIONS

In summary, the work funded by the DOE MSR Campaign at INL resulted in an expansive framework for multiphysics and multiscale analysis of MSRs shown in Figure 1-2. The special focus of the framework was to perform chemical species transport analyses shown in Figure 1-1 and detailed in the results in Sections 4–6.

Three specific steps were accomplished, enabling new and novel chemical species-transport analyses:

1. **Depletion-driven thermochemistry (Griffin + Thermochemica):** Zero-dimension multiregion (i.e., reactor loop and off-gas system) depletion with isotopic removal in Griffin, informed by chemical speciation at each time step via chemical-equilibrium calculations done in Thermochemica.
2. **Spatially resolved thermochemistry (Pronghorn + Thermochemica):** Spatially resolved equilibrium chemistry calculations by Thermochemica with given temperature, pressure, and element distributions calculated by Pronghorn.
3. **Depletion-driven, spatially resolved thermochemistry (Griffin + Pronghorn + Thermochemica):** Spatially resolved depletion and chemistry by superimposing long-lived and well-mixed (i.e., homogenous) nuclides/elements calculated by Griffin depletion and medium-lived nuclides with spatial dependence calculated by Pronghorn.

Previously inaccessible analyses were identified in Table 1-1 and can now be modeled as applications of the multiphysics framework for MSRs. Future steps to validate, enhance, and use the existing framework in FY-24 were identified to accelerate MSR reactor deployment.

In conclusion, this work, and the continuation of this work, opens doors to cross collaboration with members in the MSR campaign and drives future collaboration with industry through the novel modeling and simulation that it enables. These collaborations will ultimately build experimental MSR demonstrations in the near term and revolutionize the nuclear industry.

## 9. REFERENCES

1. Walker, S. A., M. Tano, and A. Abou-Jaoude. 2023a. “Leveraging Coupled Thermochemical Depletion Capabilities to Evaluate Off Gas and Source Term Characterization in Molten Salt Reactor Systems.” In proceedings of the International Congress on Advances in Nuclear Power Plants (ICAPP 2023), Gyeongju, South Korea, April 23–27.
2. Walker, S. A., M. Tano, and A. Abou-Jaoude. 2023b “Depletion-driven thermochemistry of molten salt reactors: review, method, and analysis.” *Frontiers in Nuclear Engineering*. 2: 1214727. <https://doi.org/10.3389/fnuen.2023.1214727>.
3. Walker, S. A., M. Tano, and A. Abou-Jaoude. 2023c. “A Coupled Griffin and Thermochemica Method for Redox Potential Control and Off-Gas Analysis During Depletion in Molten Salt Reactors.” In proceedings of the International Conference on Mathematics and Computational Methods Applied to Nuclear Science and Engineering (M&C 2023), Niagara Falls, Ontario, Canada, August 13–17.
4. Walker, S. A., et al. 2023. “Spatially Resolved Thermochemistry with Chemical Species Tracking in Molten Salt Reactors.” In *Transactions of the American Nuclear Society Winter Meeting 2023*, Washington D.C., November 12–15.

5. Olander, D. 2002. "Redox condition in molten fluoride salts: Definition and control." *Journal of Nuclear Materials* 300(2–3): 270–272. [https://doi.org/10.1016/S0022-3115\(01\)00742-5](https://doi.org/10.1016/S0022-3115(01)00742-5).
6. Kelleher, B. C. 2015. "Purification and Chemical Control of Molten Li<sub>2</sub>BeF<sub>4</sub> for a Fluoride Salt Cooled Reactor." University of Wisconsin-Madison, Madison, WI. <https://ui.adsabs.harvard.edu/abs/2015PhDT.....91K/abstract>.
7. Baes, C. F., Jr. 1965. "The Chemistry And Thermodynamics of Molten Salt Reactor Fluoride Solutions." Oak Ridge National Laboratory, Oak Ridge, TN, 1965. <https://doi.org/10.2172/4576123>.
8. Haubenreich, P. N., and J. R. Engel. 1970. "Experience with the Molten-Salt Reactor Experiment." *Nuclear Applications and Technology* 8(2): 118–136. <https://doi.org/10.13182/NT8-2-118>.
9. Shaffer, J. H. 1971. "Preparation And Handling Of Salt Mixtures For The Molten Salt Reactor Experiment." Oak Ridge National Laboratory, Oak Ridge, TN. <https://doi.org/10.2172/4074869>.
10. Zhang, J., et al. 2018. "Redox potential control in molten salt systems for corrosion mitigation." *Corrosion. Science* 144: 44–53. <https://doi.org/10.1016/j.corsci.2018.08.035>.
11. Baes, C. F., Jr. 1974. "The chemistry and thermodynamics of molten salt reactor fuels." *Journal of Nuclear Materials* 51(1): 149–162. [https://doi.org/10.1016/0022-3115\(74\)90124-X](https://doi.org/10.1016/0022-3115(74)90124-X).
12. Thoma, R. E. 1971 "Chemical Aspects Of Msre Operations." Oak Ridge National Laboratory, Oak Ridge, TN. <https://doi.org/10.2172/4675946>.
13. Permann, C. J. et al. 2020. "MOOSE: Enabling massively parallel multiphysics simulation." *SoftwareX* 11: 100430. <https://doi.org/10.1016/j.softx.2020.100430>.
14. Lee, C., et al. 2021. "Griffin Software Development Plan." ANL/NSE-21/23, INL/EXT-21-63185, Argonne National Laboratory, Lemont, IL, and Idaho National Laboratory, Idaho Falls, ID. <https://doi.org/10.2172/1845956>.
15. Balesetra, P., et al. 2020. "Coupled Multiphysics Simulation of Pool-Type Molten Salt Reactors Using Griffin/Pronghorn." In *Transactions of the American Nuclear Society Winter Meeting 2023*, Virtual, November 16–19. <http://dx.doi.org/10.13182/T123-33466>.
16. Fang, J., et al. 2020. "SAM Enhancements and Model Developments for Molten-Salt-Fueled Reactors." ANL/NSE-20/66, Argonne National Laboratory, Lemont, IL. <https://doi.org/10.2172/1763728>.
17. Piro, M. H. A., et al. 2013. "The thermochemistry library Thermochemica." *Computational Materials Science*, 67: 266–272. <https://doi.org/10.1016/j.commatsci.2012.09.011>.
18. McMurray, J., et al. 2021. "Integration Roadmap for Multi-Scale, Multi-Physics Mass Accountancy in Molten Salt Reactors." ORNL/TM-2021/1866, Oak Ridge National Laboratory, Oak Ridge, TN. <https://doi.org/10.2172/1827046>.
19. Graham, A. M., et al. 2021. "Multiphysics Coupling Methods for Molten Salt Reactor Modeling and Simulation in VERA." *Nuclear Science and Engineering* 195(10): 1065–1086. <https://doi.org/10.1080/00295639.2021.1901000>.
20. Walker, S. A., O. Calvin, M. E. Tano and A. Abou-Jaoude. 2022. "Implementation of Isotopic Removal Capability in Griffin for Multi-Region MSR Depletion Analysis." INL/CON-22-67793 in *Transactions of the American Nuclear Society Winter Meeting 2022*, Phoenix, AZ. [https://inldigitallibrary.inl.gov/sites/sti/sti/Sort\\_62761.pdf](https://inldigitallibrary.inl.gov/sites/sti/sti/Sort_62761.pdf).

21. Novak, A. J., et al. 2021. “Pronghorn: A multidimensional Coarse-Mesh Application for Advanced Reactor Thermal Hydraulics.” *Nuclear Technology* 207(7): 1015–1046. <https://doi.org/10.1080/00295450.2020.1825307>.
22. Abou-Jaoude, A., et al. 2021. “A workflow leveraging MOOSE transient multiphysics simulations to evaluate the impact of thermophysical property uncertainties on molten-salt reactors,” *Annals of Nuclear Energy* 163: 108546. <https://doi.org/10.1016/j.anucene.2021.108546>.
23. Giudicelli, G., et al. 2023. “The Virtual Test Bed (VTB) Repository: A library of reference reactor models using NEAMS tools.” *Nuclear Science and Engineering* 197(8): 2217–2233. <https://doi.org/10.1080/00295639.2022.2142440>.
24. Poschmann, M., P. Bajpai, B. W. N. Fitzpatrick and M. H. A. Piro. 2021. “Recent developments for molten salt systems in Thermochemica.” *Calphad* 75: 102341. <https://doi.org/10.1016/j.calphad.2021.102341>.
25. Martineau, R. C. 2021. “The MOOSE Multiphysics Computational Framework for Nuclear Power Applications: A Special Issue of *Nuclear Technology*.” *Nuclear Technology* 207(7): iii–viii. <https://doi.org/10.1080/00295450.2021.1915487>.
26. Pelton, A. D., P. Chartrand, and G. Eriksson. 2001. “The modified quasi-chemical model: Part IV. Two-sublattice quadruplet approximation.” *Metallurgical and Materials Transactions A* 32: 1409–1416. <http://dx.doi.org/10.1007/s11661-001-0230-7>.
27. Ard, J. C., et al. 2022. “Development of the *Molten Salt Thermal Properties Database* – Thermochemical (MSTDB-TC), example applications, and LiCl-RbCl and UF<sub>3</sub>-UF<sub>4</sub> system assessments.” *Journal of Nuclear Materials* 563: 153631. <https://doi.org/10.1016/j.jnucmat.2022.153631>.
28. Mourogov, A., and P. M. Bokov. 2006. “Potentialities of the fast spectrum molten salt reactor concept: REBUS-3700.” *Energy Conversion and Management* 47(11): 2761–2771. <https://doi.org/10.1016/j.enconman.2006.02.013>.
29. Aufiero, M., et al. 2013. “An extended version of the SERPENT-2 code to investigate fuel burnup and core material evolution of the Molten Salt Fast Reactor.” *Journal of Nuclear Materials* 441(1–3): 473–486. <https://doi.org/10.1016/j.jnucmat.2013.06.026>.
30. Besmann, T. M., and J. Schorne-Pinto. 2021. “Developing Practical Models of Complex Salts for Molten Salt Reactors.” *Thermo* 1: 168–178. <http://dx.doi.org/10.20944/preprints202106.0110.v1>.
31. McMurray, J., et al. 2021. “Roadmap for thermal property measurements of Molten Salt Reactor systems.” ORNL/SPR-2020/1865, Oak Ridge National Laboratory, Oak Ridge, TN. <https://info.ornl.gov/sites/publications/Files/Pub150500.pdf>.
32. Guo, S., J. Zhang, W. Wu and W. Zhou. 2018. “Corrosion in the molten fluoride and chloride salts and materials development for nuclear applications.” *Progress in Materials Science* 97: 448–487. <https://doi.org/10.1016/j.pmatsci.2018.05.003>.
33. Bennet, S. 2001. “The past of pid controllers.” *Annual Reviews in Control* 25: 45–53. [https://doi.org/10.1016/S1367-5788\(01\)00005-0](https://doi.org/10.1016/S1367-5788(01)00005-0).
34. Walker, S. A., and W. Ji. 2021. “Species transport analysis of noble metal fission product transport, deposition, and extraction in the molten salt reactor experiment.” *Annals of Nuclear Energy* 158: 108250. <https://doi.org/10.1016/j.anucene.2021.108250>.
35. Shayan, S., et al. 2022. “Survey of Relevant Data from the MSRP to Guide Development of MSR Chemistry Modeling Benchmarks.” ANL/NSE-22/89, Argonne National Laboratory, Lemont, IL. <https://doi.org/10.2172/1962308>.

36. Humphries, L. L., et al. 2017. "MELCOR computer code manuals." SAND2017-0876 O, Sandia National Laboratory, Albuquerque, NM.
37. Tano, M., S. A. Walker, and A. Abou-Jaoude. 2023a. "Nek5000-Pronghorn-SAM multiscale modeling of pool-type Molten Salt Reactors." In proceedings of the 20th International Topical Meeting on Nuclear Reactor Thermal Hydraulics, Washington, D.C., August 20–25.
38. Tano, M., S. A. Walker, and A. Abou-Jaoude. 2023b. "Flow-Informed Corrosion in Molten Salts using the Poisson-Nernst-Planck Model." In proceedings of the 20th International Topical Meeting on Nuclear Reactor Thermal Hydraulics, Washington, D.C., August 20–25.